Unraveling the mechanisms and implications of a stronger mid-Pliocene AMOC in PlioMIP2

Julia E. Weiffenbach[1], Michiel L.J. Baatsen[1], Henk A. Dijkstra[1,2], Anna S. von der Heydt[1,2], Ayako Abe-Ouchi[3], Esther C. Brady[4], Wing-Le Chan[3], Deepak Chandan[5], Mark A. Chandler[6], Camille Contoux[7], Ran Feng[8], Chuncheng Guo[9], Zixuan Han[10,11], Alan M. Haywood[12], Qiang Li[11], Xiangyu Li[13], Gerrit Lohmann[14, 15], Daniel J. Lunt[16], Kerim H. Nisancioglu[17,18], Bette L. Otto-Bliesner[4], W. Richard Peltier[5], Gilles Ramstein[7], Linda E. Sohl[6], Christian Stepanek[14], Ning Tan[7,19], Julia C. Tindall[12], Charles J. R. Williams[16,20], Qiong Zhang[11], and Zhongshi Zhang[9,13]

[1]Institute for Marine and Atmospheric research Utrecht (IMAU), Department of Physics, Utrecht University, 3584 CC Utrecht, The Netherlands
[2]Centre for Complex Systems Science, Utrecht University, 3584 CE Utrecht, the Netherlands
[3]Atmosphere and Ocean Research Institute, The University of Tokyo, Kashiwa, 277-8564, Japan
[4]National Center for Atmospheric Research, (NCAR), Boulder, CO 80305, USA
[5]Department of Physics, University of Toronto, Toronto, M5S 1A7, Canada
[6]CCSR/GISS, Columbia University, New York, NY 10025, USA
[7]Laboratoire des Sciences du Climat et de l'Environnement, LSCE/IPSL, CEA-CNRS-UVSQ Université Paris-Saclay, 91191 Gif-sur-Yvette, France
[8]Department of Geosciences, College of Liberal Arts and Sciences, University of Connecticut, Storrs, CT 06033, USA
[9]NORCE Norwegian Research Centre, Bjerknes Centre for Climate Research, 5007 Bergen, Norway
[10]College of Oceanography, Hohai University, Nanjing, China
[11]Department of Physical Geography and Bolin Centre for Climate Research, Stockholm University, Stockholm, 10691, Sweden
[12]School of Earth and Environment, University of Leeds, Woodhouse Lane, Leeds, West Yorkshire, LS2 9JT, UK
[13]Department of Atmospheric Science, School of Environmental studies, China University of Geoscience, Wuhan 430074, China
[14]Alfred-Wegener-Institut – Helmholtz-Zentrum für Polar and Meeresforschung (AWI), 27570 Bremerhaven, Germany
[15]Department of Environmental Physics and MARUM, University of Bremen, 28359 Bremen, Germany
[16]School of Geographical Sciences, University of Bristol, Bristol, BS8 1SS, UK
[17]Bjerknes Centre for Climate Research, Department of Earth Science, University of Bergen, 5007 Bergen, Norway
[18]Centre for Earth Evolution and Dynamics, University of Oslo, 0315 Oslo, Norway
[19]Key Laboratory of Cenozoic Geology and Environment, Institute of Geology and Geophysics, Chinese Academy of Sciences, Beijing 100029, China
[20]NCAS-Climate, Department of Meteorology, University of Reading, RG6 6ET Reading, UK

Correspondence: Julia E. Weiffenbach (j.e.weiffenbach@uu.nl)

Abstract. The mid-Pliocene warm period (3.264–3.025 Ma) is the most recent geological period in which the atmospheric CO_2 concentration was approximately equal to the concentration we measure today (ca. 400 ppm). Sea surface temperature (SST) proxies indicate above-average warming over the North Atlantic in the mid-Pliocene with respect to the pre-industrial period, which may be linked to an intensified Atlantic Meridional Overturning Circulation (AMOC). Earlier results from the Pliocene Model Intercomparison Project Phase 2 (PlioMIP2) show that the ensemble simulates a stronger AMOC in the mid-

Pliocene than in the pre-industrial. However, no consistent relationship between the stronger mid-Pliocene AMOC and either the Atlantic northward ocean heat transport (OHT) or average North Atlantic SSTs has been found. In this study, we look further into the drivers and consequences of a stronger AMOC in mid-Pliocene compared to pre-industrial simulations in PlioMIP2. We find that all model simulations with a closed Bering Strait and Canadian Archipelago show reduced freshwater transport from the Arctic Ocean into the North Atlantic. ~~The resulting~~ This contributes to an increase in salinity in the subpolar North Atlantic and Labrador Sea ~~drives~~ that can be linked to the stronger AMOC in the mid-Pliocene. To investigate the dynamics behind the ensemble's variable response of the total Atlantic OHT to the stronger AMOC, we separate the Atlantic OHT into two components associated with either the overturning circulation or the wind-driven gyre circulation. While the ensemble mean of the overturning component is increased significantly in magnitude in the mid-Pliocene, it is partly compensated by a reduction of the gyre component in the northern subtropical gyre region. This indicates that the lack of relationship between the total OHT and AMOC is due to changes in OHT by the subtropical gyre. The overturning and gyre components should therefore be considered separately to gain a more complete understanding of the OHT response to a stronger mid-Pliocene AMOC. In addition, we show that the AMOC exerts a stronger influence on North Atlantic SSTs in the mid-Pliocene than in the pre-industrial, providing a possible explanation for the improved agreement of the PlioMIP2 ensemble mean SSTs with reconstructions in the North Atlantic.

1 Introduction

At a CO_2 concentration similar to today (ca. 400 ppm) (Seki et al., 2010; Pagani et al., 2010; Badger et al., 2013; Haywood et al., 2016; de la Vega et al., 2020), the mid-Pliocene warm period (mPWP, 3.264–3.025 Ma) is the most recent geological period of sustained warmth. The mid-Pliocene climate features global surface temperatures that were roughly 3°C higher than in the pre-industrial, substantially smaller ice sheets and a reduced meridional temperature gradient (Haywood et al., 2013b, 2020). Many mid-Pliocene boundary conditions, such as the geographic position of the continents and oceans, were similar to the present day. Studying the mid-Pliocene climate can therefore provide us with knowledge that is highly relevant to understanding climate dynamics in a near future greenhouse climate (Burke et al., 2018; Tierney et al., 2019).

One component of the mid-Pliocene climate system that is of particular interest is the Atlantic Meridional Overturning Circulation (AMOC). The AMOC is an essential mechanism of poleward heat transport and has a profound impact on the global climate system. It has been linked to many other components of the climate system, such as precipitation, average Northern Hemisphere temperatures, and North Atlantic storm tracks (Jackson et al., 2015). Future projections predict a decline in the AMOC as a ~~response to global warming (Weijer et al., 2020), which~~ transient response to 21st century global warming and a possible recovery on longer timescales (Weijer et al., 2019, 2020); changes that would inevitably impact the European and North American climate (Jackson et al., 2015; Haarsma et al., 2015). ~~However,~~ When we consider the mid-Pliocene, featuring a warm climate that is considered to be in equilibrium, proxy data suggest that the mid-Pliocene AMOC was stronger than it is at present (Dowsett et al., 1992; Raymo et al., 1996; Ravelo and Andreasen, 2000). This seems to be supported by reconstruc-

tions of enhanced sea surface temperature (SST) warming in the North Atlantic in the mid-Pliocene (McClymont et al., 2020),
40 presumably linked to more northward ocean heat transport by a stronger AMOC.

The Pliocene Model Intercomparison Project Phase 2 (PlioMIP2) was initiated to gain further insight into the dynamics of the mid-Pliocene climate (Haywood et al., 2016). PlioMIP2 is an ensemble of seventeen coupled atmosphere-ocean Earth System Models that provide one mid-Pliocene simulation (mPWP; Eoi^{400}) and one pre-industrial simulation (PI; E^{280}) (Haywood
45 et al., 2016). The ensemble simulates a mid-Pliocene time slice on an interglacial peak (3.205 Ma), with an orbital forcing similar to the present day. In addition, boundary conditions such as palaeogeography and ice sheet cover were provided based on an updated reconstruction by the Pliocene Research, Interpretation and Synoptic Mapping (PRISM4) project (Dowsett et al., 2016). Important differences between the pre-industrial and mid-Pliocene boundary conditions include the closure of the Bering Strait and Canadian Archipelago as well as a strong reduction in the extent of the Greenland and West-Antarctic Ice
50 Sheet.

In this paper, we will look into the effect of a stronger mid-Pliocene AMOC on North Atlantic SSTs in the PlioMIP2 ensemble. Previous analysis on average North Atlantic SSTs and the AMOC strength led to the conclusion that the reconstructed SST warmth in the North Atlantic cannot be attributed to an intensified mid-Pliocene AMOC (Zhang et al., 2021b). However,
55 it has been shown the response of North Atlantic SSTs to the AMOC varies among coupled general circulation models (Ba et al., 2014; Kim et al., 2018) as there are many different variables that affect SSTs (Zhang et al., 2019), such as aerosols and clouds (Booth et al., 2012; Feng et al., 2019) or atmospheric stochastic forcing (Clement et al., 2015). Here, we will examine reconstructed mid-Pliocene SSTs at six sites in the North Atlantic and compare these to PlioMIP2 ensemble results. The reconstructed SSTs originate from the marine isotope KM5c timeslice (3.204-3.207 Ma), which is a warm interval in the
60 mid-Pliocene during which orbital forcing was similar to present day (Haywood et al., 2013a). Furthermore, we will investigate whether there is a difference in the degree to which the AMOC influences North Atlantic SSTs in the mid-Pliocene and pre-industrial.

In an analysis of the AMOC in the PlioMIP2 ensemble, Zhang et al. (2021b) reported a stronger AMOC in all mid-Pliocene
65 simulations compared to the pre-industral. It is likely that the strengthening ~~originates from~~ is linked to the closure of the Bering Strait and Canadian Archipelago in the mid-Pliocene. Earlier work shows that closing these Arctic gateways leads to a strengthened AMOC due to altered freshwater fluxes from the Arctic into the North Atlantic (Otto-Bliesner et al., 2017). Several PlioMIP2 model groups have identified the changes in paleogeography, specifically the Arctic gateways closure, to be the cause of a stronger simulated mid-Pliocene AMOC (Hunter et al., 2019; Chan and Abe-Ouchi, 2020; Tan et al., 2020;
70 Feng et al., 2020; Stepanek et al., 2020; Baatsen et al., 2022). In this study, we will consider whether the closure of the Arctic gateways in the mid-Pliocene ~~is the main driver behind the~~ can be linked to the stronger mid-Pliocene AMOC in the PlioMIP2 ensemble. If this is the case, changes in geographic boundary conditions may ~~present a significant forcing on~~ lead to significant changes in the forcing, which affect the AMOC strength during the mid-Pliocene~~, which~~. The AMOC should then be consid-

ered a non-analog feature for a future warm climate and a potential driving force of the mid-Pliocene climate.

75

All PlioMIP2 models simulate an intensified AMOC - but the response of the Atlantic northward ocean heat transport (OHT) to this strengthening has been shown to be inconsistent (Zhang et al., 2021b). We will look further into the OHT response by partitioning the Atlantic OHT into a component associated with the overturning circulation and a component associated with the wind-driven gyres. Classical scaling shows that the OHT of an overturning cell is linearly proportional to the strength

80 of the overturning and the temperature difference between the northward and southward flowing water in the cell (Vallis and Farneti, 2009). However, the total OHT is a sum of the heat transport associated with the overturning circulation as well as the heat transport associated with the wind-driven gyre circulation. This may explain why no one-to-one relationship has been found between the total OHT and AMOC strength in the PlioMIP2 ensemble (Zhang et al., 2021b). The wind-driven gyre OHT is closely coupled to the atmospheric heat transport (AHT) (Vallis and Farneti, 2009). This results in a complex interplay

85 between the OHT and AHT (Rose and Ferreira, 2012; Yang and Dai, 2015), and therefore also between the two components of the OHT itself, where a high degree of compensation between the two is found especially in the North Atlantic (Farneti and Vallis, 2013). It has previously been shown that this partitioning can shed light on which oceanic processes are dominating the OHT, thereby also identifying possible consequences for the climate system (Ferrari and Ferreira, 2011; Yang et al., 2015)

90 In Section 2, we will ~~first~~ introduce the PlioMIP2 models and the methods used to analyze the mid-Pliocene AMOC. ~~We show results of our analysis of the mid-Pliocene North Atlantic SSTs in~~ In Section 3.1, ~~followed by an illustration of how changes in~~ we start by addressing the question that has been raised in earlier studies: whether relatively high SSTs in the North Atlantic can be linked to a stronger AMOC in the mid-Pliocene (e.g. Dowsett et al., 2013; Haywood et al., 2020). We follow with an analysis of what may be causing the strengthened AMOC by looking at changes in salinity and the freshwater transport

95 and ~~salinity drive a stronger mid-Pliocene AMOC compared to the pre-industrial~~ surface freshwater flux in Section 3.2. ~~Next,~~ Then we will study the consequences of ~~a~~ the stronger mid-Pliocene AMOC in PlioMIP2 in Section 3.3, specifically how this affects OHT by the overturning circulation ~~(Section 3.3)~~ and transports by the subtropical gyre~~(Section 3.4)~~. We will provide a discussion of our results in Section 4 and present our conclusions in Section 5.

2 Data and methods

2.1 PlioMIP2 models

For this study, complete datasets for analysis are available from 15 out of 17 models participating in PlioMIP2. The models are listed in Table 1 along with their institute and reference to the individual model description. All models have performed a pre-industrial (E^{280}) simulation at a CO_2 concentration of 280 ppm (models participating in CMIP6 at 284.3 ppm, see Table 1) and a mid-Pliocene (Eoi^{400}) simulation at a CO_2 concentration of 400 ppm and with boundary conditions implemented as

105 described in Haywood et al. (2016). The exception is HadGEM3, where the pre-industrial land-sea mask and bathymetry is also used in the mid-Pliocene simulation (Williams et al., 2021). For this reason, the model is excluded from any multi-model

Table 1. Overview of PlioMIP2 models used in this study.

Model name	Institute	Simulation length (years)[3]		Reference
		PI	mPWP	
CCSM4	NCAR, USA	>1000	1100	Feng et al. (2020)
CCSM4-UoT	University of Toronto, Canada	4630	1250	Chandan and Peltier (2017)
CCSM4-Utr	IMAU, Utrecht University, The Netherlands	3100	2048	Baatsen et al. (2022)
CESM1.2	NCAR, USA	>1000	1200	Feng et al. (2020)
CESM2[1]	NCAR, USA	1200	1500	Feng et al. (2020)
COSMOS	AWI, Germany	1950	1950	Stepanek et al. (2020)
EC-Earth3-LR[1]	Stockholm University, Sweden	1500	1600	Zhang et al. (2021a)
GISS2.1G[1]	GISS, USA	5000	3100	-
HadCM3	University of Leeds, UK	2999	2499	Hunter et al. (2019)
HadGEM3[1,2]	University of Bristol, UK	2050	576	Williams et al. (2021)
IPSL-CM5A	LSCE, France	>800	3680	Tan et al. (2020)
IPSL-CM5A2	LSCE, France	1500	3480	Tan et al. (2020)
IPSL-CM6A[1]	LSCE, France	1100	1460	Lurton et al. (2020)
MIROC4m	JAMSTEC, Japan	2220	3000	Chan and Abe-Ouchi (2020)
NorESM1-F[1]	BCCR, Norway	2000	500	Li et al. (2020)

[1] CMIP6 model with pre-industrial 1850 CO_2 at 284.3 ppm.

[2] Pre-industrial land-sea mask in both simulations.

[3] As presented in Zhang et al. (2021b).

mean (MMM) and ensemble standard deviation calculations. It is included in figures with individual model results and shown as an unfilled marker in scatter plots. It serves as an additional reference of a model with higher than pre-industrial CO_2 levels but limited geographic changes.

2.2 Proxy data

To compare mid-Pliocene model results with reconstructed data, we use SST proxy data from a 30k year interval centered on the KM5c time slice by Foley and Dowsett (2019) and McClymont et al. (2020). The PRISM4 dataset (Foley and Dowsett, 2019) is a collection of $U^{k'}_{37}$ proxies (calibrated using the Müller et al. (1998) method). The dataset by McClymont et al. (2020) includes

both $U_{37}^{k'}$ proxies (calibrated using the BAYSPLINE method) as well as foraminifera Mg/Ca proxy SST reconstructions. In this study, SST reconstructions from six different sites between 30°N and 70°N in the North Atlantic have been used. For comparison to model anomalies, the NOAA ERSST5 dataset (Huang et al., 2017) for the years 1870-1899 is used as the observational pre-industrial SST dataset.

2.3 Data analysis

All models except IPSL-CM5A and IPSL-CM5A2 have provided 100 years of annual model data for both E^{280} and Eoi^{400}. IPSL-CM5A and IPSL-CM5A2 have provided 50-year averages only, so they are excluded from analysis that requires annual data.

Percentage differences between the mid-Pliocene and pre-industrial are computed relative to the pre-industrial. An anomaly is defined as the difference between the mid-Pliocene and pre-industrial (mPWP-PI; Eoi^{400}-E^{280}), unless stated otherwise. Standard deviations of individual model means are calculated using annual data. Standard deviations of MMM anomalies are calculated using the individual model Eoi^{400}-E^{280} anomalies.

Data provided by individual modelling groups includes the ocean potential temperature, ocean meridional velocity, ocean salinity, the Atlantic meridional streamfunction, the total Atlantic OHT and the atmospheric zonal and meridional wind at 1000 hPa. In addition, the atmospheric surface freshwater flux (precipitation minus evaporation; PmE) fields for all models provided by Han et al. (2021) have been used. SST, SSS, PmE and atmospheric wind fields have been interpolated to a ~~1°x1°~~ $1° \times 1°$ regular grid using bilinear interpolation. All calculations for Atlantic ocean heat transport and freshwater transport have been performed on model native grids, except for COSMOS where it is done on the regular interpolated grid. These computations have been done using Atlantic region masks provided by the individual modelling groups. The mean AMOC strength is calculated from the 100-yr mean Atlantic meridional overturning streamfunction and the yearly AMOC strength from the annual mean Atlantic meridional overturning streamfunction. The AMOC strength is defined as the maximum value of the Atlantic meridional overturning streamfunction north of the equator and below 500 m depth. Potential density is calculated from potential temperature and salinity using the TEOS-10 equation of state (Roquet et al., 2015).

2.3.1 Ocean heat transport

The 100-year mean OHT is defined at every latitude y as:

$$OHT = \rho_0 c_p \int \int_{x_E}^{x_W} vT \overline{vT} \, dx \, dz \tag{1}$$

Here, v is the meridional ocean velocity and T the ocean potential temperature of each grid cell of dx in longitude and dz in depth; the bar denotes a 100-year mean. The y-dependency of the OHT is omitted in the notation. For the Atlantic OHT, integration is performed zonally between the eastern and western ~~bounds~~ boundaries of the Atlantic Ocean, respectively

x_E and x_W. The constants ρ_0 and c_p are the average density and specific heat of sea water, respectively. These are set at $\rho_0 = 1.026 \cdot 10^{-3}$ kg cm^{-3} and $c_p = 3996$ J K kg^{-1}. In this study, the total OHT is calculated from the 100-year mean 3D meridional heat transport ($\overline{vT}$) field. This total OHT can be partitioned into a mean flow OHT^M and a transient component OHT^T (Viebahn et al., 2016):

$$OHT = OHT^M + OHT^T \tag{2}$$

where the time mean component OHT^M and transient component OHT^T are

$$OHT^M = \rho_0 c_p \int \int_{x_E}^{x_W} \overline{v}\,\overline{T} \, dx \, dz \tag{3}$$

$$OHT^T = \rho_0 c_p \int \int_{x_E}^{x_W} \overline{v'T'} \, dx \, dz \tag{4}$$

Here, $v = \overline{v} + v'$ and $T = \overline{T} + T'$ where $\overline{v}$ and $\overline{T}$ are the 100-year mean and v' and T' the transient components of the respective v and T fields. As the 100-year mean $\overline{vT}$, $\overline{v}$ and $\overline{T}$ are available ~~as~~ from the model output, this allows us to deduce $\overline{v'T'}$.

Next, we are able to separate OHT^M from (3) into two separate components associated with either the zonal mean flow or the azonal flow. This will approximately separate OHT^M in heat transport that can be attributed to the overturning circulation (i.e. the zonal mean flow) and heat transport that results from wind-driven gyre circulation (i.e. the azonal flow).

$$OHT^M = OHT_{ov} + OHT_{az} \tag{5}$$

Following Dijkstra (2007) and Viebahn et al. (2016):

$$OHT_{ov} = \rho_0 c_p \int \int_{x_E}^{x_W} \langle \overline{v} \rangle \langle \overline{T} \rangle \, dx \, dz \tag{6}$$

$$OHT_{az} = \rho_0 c_p \int \int_{x_E}^{x_W} \langle \overline{v}^* \overline{T}^* \rangle \, dx \, dz \tag{7}$$

Here, $\langle \overline{v} \rangle$ and $\langle \overline{T} \rangle$ are the zonal average of $\overline{v}$ and $\overline{T}$, and $\overline{v}^*$ and $\overline{T}^*$ are the azonal components such that $\overline{v} = \langle \overline{v} \rangle + \overline{v}^*$ and $\overline{T} = \langle \overline{T} \rangle + \overline{T}^*$.

This ~~separation into overturning and gyre components can~~ method for separating the ocean heat transport into a component that can be attributed to the overturning circulation and a component attributed to the wind-driven gyre circulation is a conventional method introduced by Bryan (1982) and Hall and Bryden (1982). It has been used in many studies of both observational (e.g., Johns et al., 2011) and model data (e.g., Viebahn et al., 2016). That said, it is important to recognise that it does not

perfectly separate the transport by the gyre circulation and overturning circulation. Attributing all zonal mean circulation to the overturning circulation and all azonal flow to the gyre circulation is a simplification that inevitably introduces some error. An alternative method that may resolve problems with separating the overturning and gyre components near the western boundary and prevents the deep ocean circulation from being attributed to the wind-driven gyre could be to separate out transport by the western boundary current of the gyre circulation and attribute heat transport in the deep ocean to the overturning circulation only. This requires a definition of the deep ocean, which could be achieved by identifying the level of no motion along the vertical axis and assigning all grid points below this level to the deep ocean. For the western boundary current, a longitude for the western boundary could be determined by integrating the meridional volume transport above the level of no motion from east to west until the total volume transport is zero. Heat transport east of this boundary and above the level of no motion can then be attributed to the gyre circulation and the rest of the heat transport to the overturning circulation. The reason why we have not implemented this method is that it introduces new problems and error due to challenges in accurately defining the boundary of the deep ocean and western boundary, in particular because the method has to be implemented for every model individually. Alternatively, a method that involves separating these components based on water mass ventilation, as done by Talley (2003), would also be interesting to implement as it is more accurate and would therefore allow for a more quantitative assessment of the error introduced by our method. However, the implementation of this method is complex, especially when it has to be carried out for each individual model, rendering it beyond the scope of this study.

It should be noted that the separation for the overturning and gyre components as shown above can only be done for the time mean component as instantaneous velocity fields are not available. Therefore, the total OHT will always contain a transient component OHT^T in addition to the mean overturning OHT_{ov} and gyre components OHT_{az}:

$$OHT = OHT_{ov} + OHT_{az} + OHT^T \tag{8}$$

The variability contained in the transient component OHT^T is primarily a result of the seasonal cycle and is therefore largely unaffected by the choice of averaging period (Viebahn et al., 2016). Only in areas of high eddy activity, primarily the Southern Ocean, the transient component is significant (Yang et al., 2015). Supplementary ~~figure~~ Figure S1 shows a comparison between the total Atlantic OHT (OHT) and the time mean Atlantic OHT ($OHT^M = OHT_{ov} + OHT_{az}$), where no significant discrepancy is found for most models. The exceptions are the COSMOS, HadCM3, GISS2.1G, MIROC4m and NorESM1-F. In COSMOS and HadCM3, this difference most likely occurs as a result of using surface heat fluxes at the sea surface to calculate the total OHT. As this approach requires assuming that there is no change in ocean heat storage and that all heat that vertically enters the ocean through the surface will be transported horizontally by the circulation (Yang et al., 2015), this may indicate that either or both of these conditions are not fulfilled in these models. For COSMOS, the absence of thermal equilibrium has been explicitly shown by Stepanek et al. (2020) and Lohmann et al. (2022). Therefore, we have used OHT^M that is calculated from the individual velocity and temperature fields as the total OHT for COSMOS and HadCM3. In addition, the calculated overturning OHT component from MIROC4m and COSMOS is quite noisy due to interpolation in the original velocity, temperature or region fields. This output is smoothed using a 5° running mean.

For models with a curvilinear grid, the transport calculations on a native grid lead to a degree of error at higher latitudes due to the disalignment of the meridional velocity with the y-direction of the grid cells. For this reason, the OHT components are only calculated up to 65°N for all models.

2.3.2 Freshwater transport

210 The freshwater transport F is calculated for all ~~models~~ model simulations using the 100-year mean meridional ocean velocity $\overline{v}$ and salinity $\overline{S}$ fields:

$$F = -\frac{1}{S_0} \int \int \overline{v}(\overline{S} - S_0)\, dx\, dz \tag{9}$$

where S_0 is the reference salinity, which is set to be the average Atlantic Ocean salinity for every individual simulation. The integration is performed over the ocean depth and Atlantic basin width as for the Atlantic OHT and calculated up to 65°N due

215 to curving of curvilinear grids. The freshwater transport is also calculated for two sections of the Atlantic Ocean at 62°N west and east of Greenland, respectively referred to the Labrador Sea and Greenland Scotland Ridge (GSR) freshwater transports. Freshwater transport through the Bering Strait in the pre-industrial simulations is also computed.

In order to analyze the separate effect of the overturning and wind-driven gyre circulation on the Atlantic freshwater trans-

220 port, the same separation of components is done as for the OHT, following Dijkstra (2007):

$$F_{ov} = -\frac{1}{S_0} \int \int \langle \overline{v} \rangle (\langle \overline{S} \rangle - S_0)\, dx\, dz \tag{10}$$

$$F_{az} = -\frac{1}{S_0} \int \int \langle \overline{v}^* \overline{S}^* \rangle\, dx\, dz \tag{11}$$

~~The~~ This means that a similar degree of error is introduced when separating the freshwater transport into the overturning and a gyre component as was discussed above for the separation of the OHT components. In addition, total freshwater transport

225 does not include the transient term in our study due to the use of 100-year mean velocity and salinity fields. This transient term is caused by seasonal variations in gyre circulation, similar to the transient OHT component, and surface salinity as well as baroclinic mesoscale eddies at the boundary of the subtropical and subpolar gyres (Treguier et al., 2012). We neglect the transient term, as it was shown to be small at a model resolution of approximately 1° (Jüling et al., 2021).

3 Results

230 Figure 1 gives an overview of the AMOC strength and its variability in the individual mid-Pliocene and pre-industrial simulations. We find that all models except CESM1.2 and HadGEM3 simulate a stronger AMOC in the Pliocene. This is a slightly different result from Zhang et al. (2021b), where CESM1.2 did simulate a stronger AMOC in the Pliocene. Discrepancies between AMOC strength reported by Zhang et al. (2021b) and Figure 1 can be attributed to a difference in the 100-year time

interval of the model data.
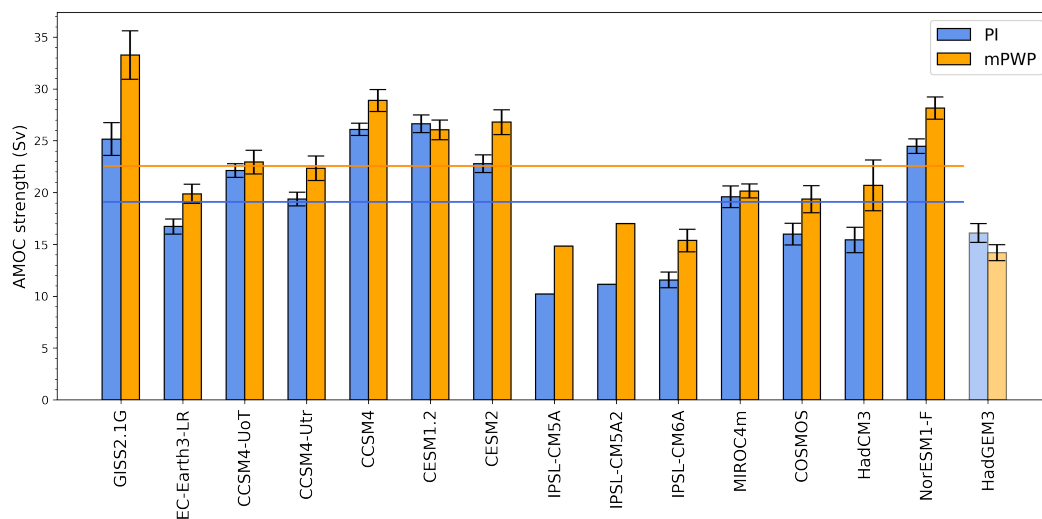
Figure 1. Individual model AMOC strength in the pre-industrial (blue) and mid-Pliocene (orange). Error bars indicate one standard deviation from the time-mean AMOC strength computed using 100 years of yearly data. The horizontal lines indicate the multi-model mean AMOC strength.

The error bars in Figure 1 show the standard deviation of the annual AMOC strength from the 100-year mean. The error bars for CESM1.2 show that the decrease in AMOC strength is not significant. This is also the case for the increase in AMOC strength in CCSM4-UoT and MIROC4m. For all other models included in this study, the intensified AMOC in the mid-Pliocene compared to the pre-industrial is significant. The only model simulating a significant decrease in AMOC strength is HadGEM3, presumably related to the pre-industrial land-sea mask configuration in the mid-Pliocene simulation as discussed in Zhang et al. (2021b). Also note that for the majority of the models, the variability in the AMOC strength increases in the mid-Pliocene, with the exception of MIROC4m and HadGEM3.

3.1 North Atlantic SSTs linked to AMOC

3.1.1 Comparison of models with proxy data

Figure 2 compares the MMM and individual models' SSTs to $U^{k'}_{37}$ SST proxy data from Foley and Dowsett (2019) and $U^{k'}_{37}$ and Mg/Ca proxy data from McClymont et al. (2020) at six different North Atlantic sites. These sites are chosen based on their location between 30-70°N, excluding sites in proximity to the Mediterranean Sea. Figure 2a shows the SSTs in the mid-Pliocene and Figure 2b the SST mPWP-PI anomalies with respect to the MMM 30°N-70°N average North Atlantic mPWP-PI SST anomaly. Red colored regions in Figure 2b indicates above average warming and blue colored regions below average warming
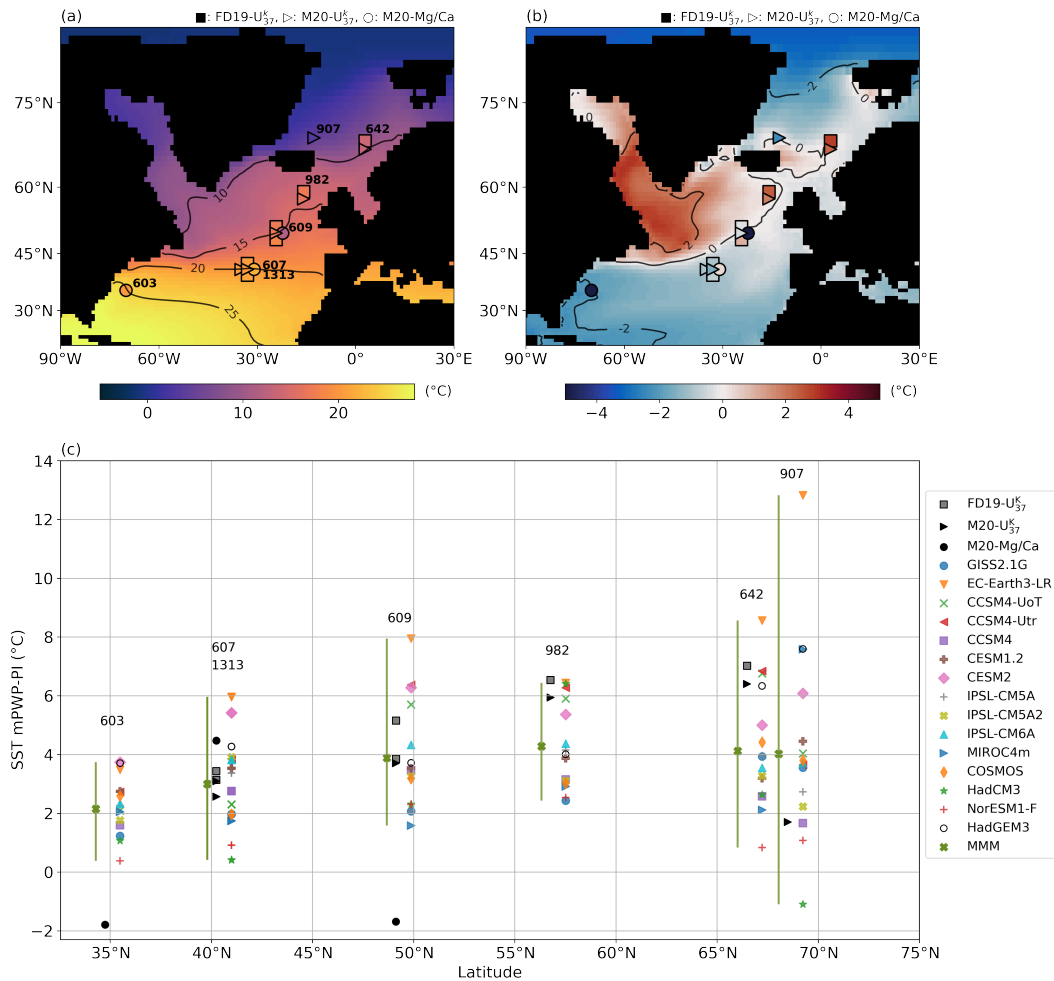
Figure 2. (a) Mid-Pliocene MMM and reconstructed North Atlantic SST. (b) MMM and reconstructed North Atlantic SST anomaly (mPWP-PI) with respect to the average MMM North Atlantic SST anomaly (30°N-70°N). (c) Individual model SSTs and reconstructed SSTs at six proxy locations in the North Atlantic. The vertical line shows the model spread and the MMM (excluding HadGEM3) is indicated by a cross. FD19-$U_{37}^{k'}$ refers to the Foley and Dowsett (2019) data, M20-$U_{37}^{k'}$ and M20-Mg/Ca to the McClymont et al. (2020) data. SST proxy anomalies are computed with pre-industrial ERSST5 data (Huang et al., 2017). The code to read and plot the proxy SST data has been adapted from Oldeman (2021)

with respect to the average 30°N-70°N North Atlantic warming. This allows for a closer inspection of regional differences in extratropical North Atlantic warming. The modelled SST values at the different proxy sites can be found in Supplementary Table S1. Figure 2b indicates that the strongest amplified North Atlantic warming in the MMM mid-Pliocene SSTs occurs north of 45°N and west of 30°W, an area where there is currently no proxy data available for the KM5c timeslice. Most proxy data originate from locations that are in the white area in Figure 2b, meaning that the warming simulated there is approximately

255

equal to the extratropical North Atlantic mean warming.

The mPWP-PI anomalies of the reconstructed SSTs and MMM SSTs are plotted in Figure 2c, along with the individual model SST anomalies. We find that the discrepancy between reconstructed and MMM SST anomalies is smallest for sites 607/1313 and 609, with the exception of the relatively cold Mg/Ca reconstruction at site 609. The sites where reconstructions indicate the strongest mid-Pliocene warming are sites 982 and 642. These sites are also the only two sites that fall within the area where MMM warming is higher than the North Atlantic 30-70°N average, as seen in Figure 2b, although they are both at the edge of this area. The sites north of 60°N show a greater discrepancy between reconstructions and the MMM, as well as a relatively large model spread. The reconstructed SST at site 603 also does not agree with the MMM and falls outside the range of model SSTs, which may be related to its location in the highly variable Gulf Stream region. This region including the Gulf Stream separation is generally not well resolved in low resolution general circulation models (Bryan et al., 2007; Saba et al., 2016; Schoonover et al., 2017). It may also be due to other factors such as calibration and seasonality affecting the Mg/Ca SST reconstructions (McClymont et al., 2020), since we see that the Mg/Ca proxy SST values are much lower than the PlioMIP2 model range at site 609 as well.

3.1.2 Effect of the stronger mid-Pliocene AMOC

Even though we observe above average warming of SSTs in the northwestern North Atlantic (Figure 2b), it has been shown that average North Atlantic temperatures do not respond consistently to a stronger mid-Pliocene AMOC (Zhang et al., 2021b). To further examine the effect of a stronger mid-Pliocene AMOC on North Atlantic SSTs, we show correlation maps between annual mean AMOC strength and SSTs at every grid point for both the pre-industrial and mid-Pliocene in Figure 3. Grid points that are colored red show positive correlation between the SST and the AMOC strength, with positive correlations greater than 0.4 indicated by a white contour line.

The majority of the PlioMIP2 models show that the effect of the AMOC on North Atlantic SSTs is different in pattern in the mid-Pliocene than in the pre-industrial, where for most models there is a relatively larger area of significant positive correlation in the mid-Pliocene (see Supplementary Table S2). Furthermore, the positive correlation with SSTs is higher in the mid-Pliocene, with the exception of CCSM4, CESM1.2, CESM2, NorESM1-F, IPSL-CM6A and HadGEM3. CCSM4 and CESM2 do not have a stronger correlation between North Atlantic SSTs and the AMOC strength, but their maps do show a shift in the spatial pattern of correlation. The same is true for HadGEM3, which does not employ a mid-Pliocene land-sea mask and simulates a weaker mid-Pliocene AMOC. In CESM1.2, which has a weaker AMOC in the mid-Pliocene, as well as NorESM1-F and IPSL-CM6A, the correlation remains similar in strength and pattern. The results suggest that for the majority of the models, the stronger mid-Pliocene AMOC exerts a stronger influence on North Atlantic SSTs than in the pre-industrial. This would imply that a stronger mid-Pliocene AMOC also corresponds to higher North Atlantic temperatures, although the extent of this . In the MMM correlation maps (Supplementary Figure S2) we see a consistent area of positive correlation in both the PI and mPWP, that increases in extent and magnitude in the mPWP. It supports our individual model results in Figure
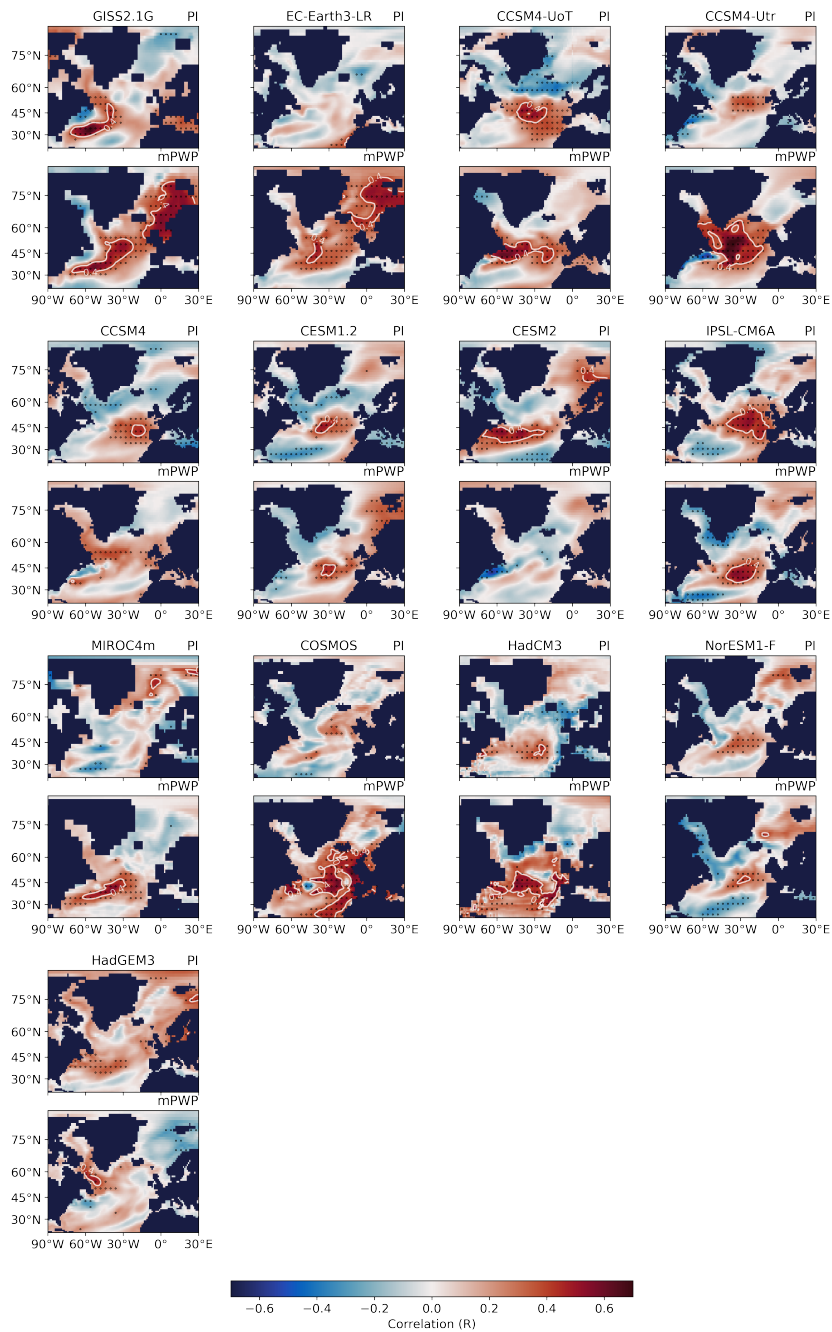
Figure 3. Correlation between the annual AMOC strength and annual SSTs for individual models. The top panel for each model shows the results for the pre-industrial and the bottom panel for the mid-Pliocene. Both the AMOC strength and SSTs have been linearly detrended before correlating. Stippling indicates significance at the 595% confidence level. White contours show a positive correlation of $R = 0.4$.

290 3, but at the same time underscores the need to stress that the relation and the specific area where ~~this is the case could be~~ a stronger mid-Pliocene AMOC may be related to higher North Atlantic temperatures appears to be highly model dependent.

3.2 ~~Density-driven~~ Density-affected increase in AMOC strength

The AMOC is known to be affected by meridional gradients in density (Rahmstorf, 1996; Thorpe et al., 2001; Stouffer et al., 2006; Wang et al., 2010) where the relatively high density in the North Atlantic is ~~considered to be a driver of~~ linked to deep
295 convection that constitutes the sinking branch of the AMOC in the high northern latitudes. ~~As the AMOC~~ It should be noted that the AMOC is driven by meridional pressure gradients that scales with $\Delta\rho H^2$ (de Boer et al., 2010), with $\Delta\rho$ the meridional density gradient and H the depth of the maximum overturning streamfunction, and that a correlation with the density gradient is only expected if the depth of the overturning is not affected by processes that are not directly related to the strength of the AMOC. Given that the AMOC becomes stronger in almost all mid-Pliocene simulations relative to the pre-industrial, we ~~expect~~
300 ~~this strengthening to scale with~~ now examine whether this is related to an increase in the meridional density gradient in Figure 4. Figure 4a shows the zonal mean MMM potential density of the top 1 km of the Atlantic Ocean, where it is clear that most of the Atlantic becomes less dense. This is also indicated by Figure 4b, where the potential density from Figure 4a is averaged over the top 1 km. However, for the higher northern latitudes, approximately 40-80°N, we observe that the potential density decreases by about 0.1 kg m^{-3}, which is substantially less than in the rest of the Atlantic where the decrease is approximately
305 0.3 kg m^{-3}. This results in an overall increase in the meridional density gradient, which is defined as the difference between the 50-70°N average and 10-30°S average ~~.~~ for all models except GISS2.1G. In this specific model, significant deep water formation takes place at latitudes higher than 70°N in the mPWP (Supplementary Figure S3) and we have therefore extended the northern box to 50-80°N for GISS2.1G. We have plotted the AMOC strength anomaly against the meridional density gradient anomaly ~~against the AMOC strength anomaly~~ for all individual models in Figure 4c. This shows a clear relationship
310 between the mPWP-PI change in density gradient and the AMOC strength, where a greater increase in density gradient ~~results in~~ correlates significantly ($R = 0.67, p = 0.01$) with a larger increase in AMOC strength. ~~A notable exception is GISS2.1G, in which deep water formation takes place at higher latitudes than 65°N and the AMOC strength is thus not strongly related to the density gradient we have defined.~~

315 Changes in density are brought about by changes in the potential temperature and salinity of the ocean. We show the potential temperature and salinity in the same manner as the potential density in Figure 4d-4f and Figure 4g-4i, respectively. As the North Atlantic becomes substantially warmer between 40-80°N than the rest of the basin in the mid-Pliocene, temperature cannot explain the increase in meridional density gradient. This leaves salinity as the main driver of the increase in the meridional density gradient, which is supported by Figures 4g-4i. We see a zonal mean freshening of the South Atlantic and tropics from
320 the surface down to approximately 500 m. The rest of the basin shows an increase in salinity, with the exception of the surface at latitudes higher than 65°N. A high salinity anomaly is found between 40-60°N in the top 100 m, extending further downwards in some locations. The salinity anomaly results in an increase in the meridional salinity gradient in the mid-Pliocene, where a relationship between the increased salinity gradient and increased AMOC strength in the mid-Pliocene is shown in Figure 4i.
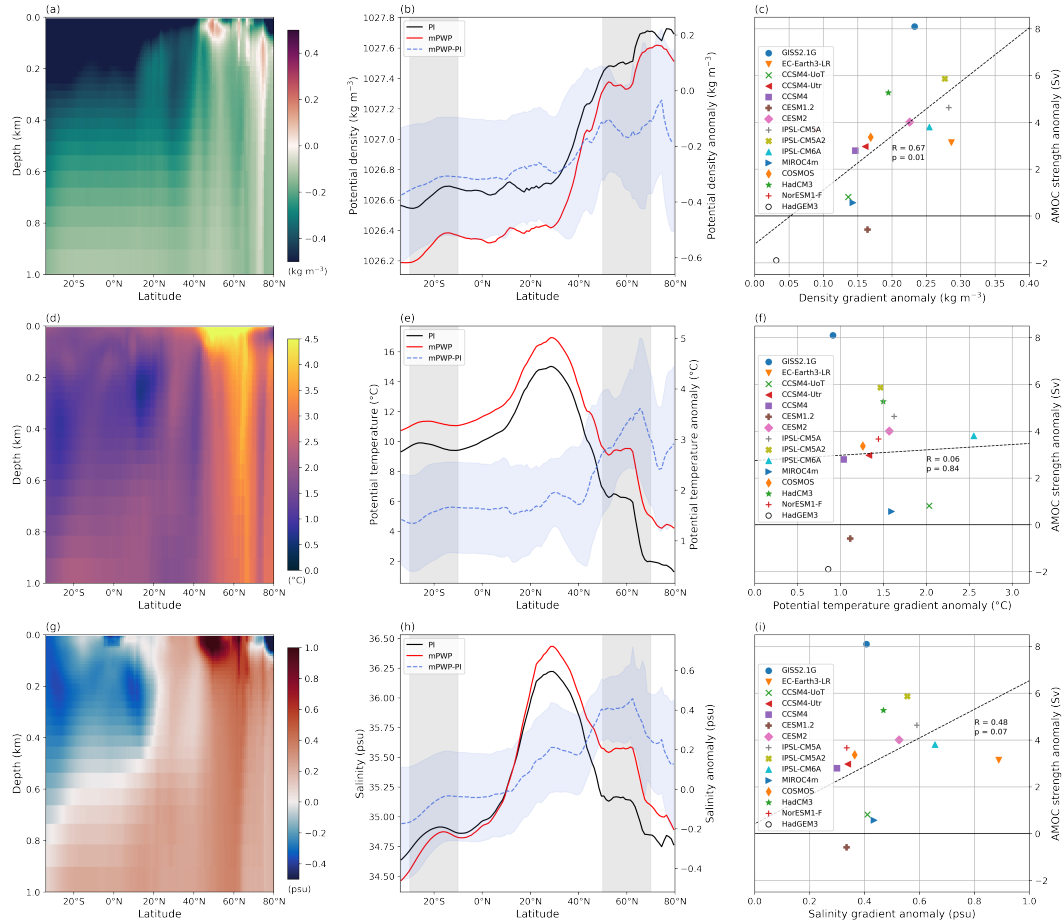
Figure 4. (a) MMM top 1 km Atlantic zonal mean potential density mPWP-PI anomaly. (b) MMM top 1 km depth-averaged Atlantic zonal mean potential density in the PI and mPWP (left y-axis) and mPWP-PI anomaly (right y-axis). ~~Shading~~ Blue shading indicates one standard deviation from the MMM by individual models. (c) Individual model mPWP-PI AMOC strength anomaly plotted against the mPWP-PI anomaly in meridional gradient of the top 1 km Atlantic potential density~~, plotted against the mPWP-PI AMOC strength anomaly~~. The meridional gradient is defined as the difference between the 50-70°N average and 10-30°S average (latitude bands are indicated by grey shading in (b)). (d)-(f) Same as (a)-(c) for potential temperature. (g)-(i) Same as (a)-(c) for salinity.

Overall, Figure 4 shows that the ~~density driven increase in~~ meridional density gradient increase affecting the AMOC strength
325 must be a result of increased salinity in the high North Atlantic. This is supported by further analysis of the northern and southern boxes in Supplementary Figure S4, which shows the correlation plots from Figure 4 for the individual boxes. There we find that density anomalies in both boxes correlate well with the AMOC strength, but that it is only in the northern box that salinity anomalies show a significant correlation with the AMOC.

3.2.1 Sea surface salinity
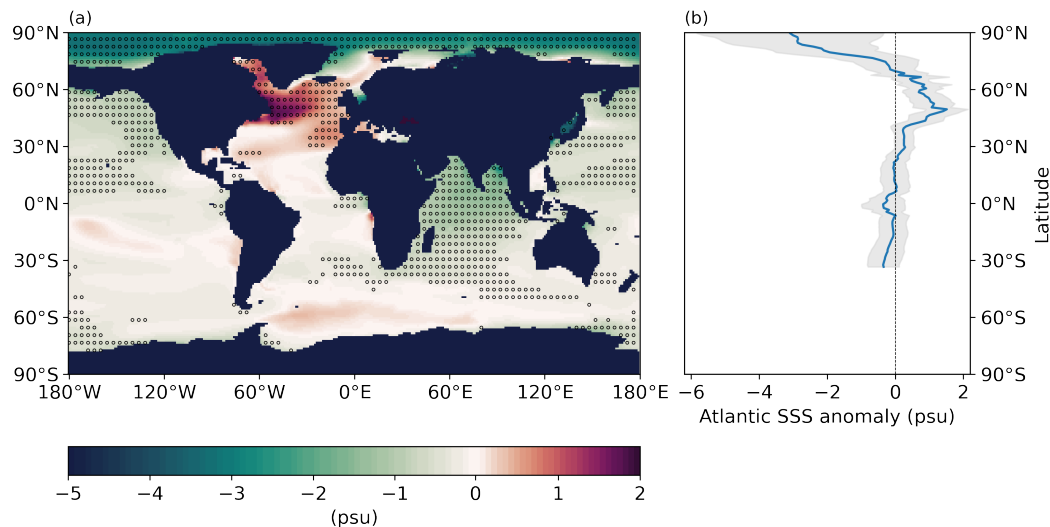
Figure 5. (a) Multi-model mean mPWP-PI difference in sea surface salinity (SSS). Stippling indicates that 12 or more models agree on the sign of the difference. (b) Atlantic zonal mean SSS anomaly, excluding the Mediterranean Sea and North Sea. The shading indicates one standard deviation from the MMM by individual models, excluding HadGEM3.

330   The consistent intensification of the mid-Pliocene AMOC across the PlioMIP2 ensemble compared to the PlioMIP1 ensemble is suggested to be linked to the closure of the Arctic gateways in PlioMIP2 (Haywood et al., 2020; Zhang et al., 2021b). Closing these Arctic gateways has been shown to cause an intensification of the AMOC through the decrease in freshwater transport from the Arctic into the North Atlantic via the Labrador Sea. This increases the salinity in the Labrador Sea and subpolar North Atlantic, thereby stimulating deep water formation in these areas (Otto-Bliesner et al., 2017). In the previous section

335   we show that there is a substantial increase in the MMM salinity in the 40-60°N latitude band in the North Atlantic. From the MMM sea surface salinity (SSS) in Figure 5a, we can identify a robust increase of approximately 2 psu in sea surface salinity in the Labrador Sea and in the North Atlantic between 40-60°N. It is exclusively at these latitudes that we find that the Atlantic zonal mean sea surface salinity anomaly to be significantly positive (Figure 5b) when considering the standard deviation of the individual models. All models forced with the PRISM4 reconstruction in the mid-Pliocene show this increase in sea surface

340   salinity, as can be seen in Supplementary Figure S5. The fact that the HadGEM3 model, using a pre-industrial land-sea mask, does not show a sea surface salinity increase in the subpolar North Atlantic or Labrador Sea strengthens the argument that the stronger mid-Pliocene AMOC can be attributed linked to the closure of the Arctic gateways in the PlioMIP2 simulations.

    Even though the Bering Strait is closed in the mid-Pliocene experiments, blocking freshwater transport from the Pacific into

345   the Atlantic Arctic Ocean, a 3-4 psu decrease in sea surface salinity in the Arctic Ocean can be seen in Figure 5a. This de-

crease is present in all models except GISS2.1G, but the extent and magnitude of the decrease is highly model dependent (Supplementary Figure S5). ~~While the closure of the Bering Strait could be expected to lead to higher~~ The decreased Arctic sea surface salinity ~~in the Arctic Ocean, we observe the opposite. This~~ may be explained by ~~earlier PlioMIP2 studies that show~~ a higher surface freshwater flux into the Arctic Ocean in the mid-Pliocene ~~(Haywood et al., 2020; Han et al., 2021)~~ as a result

350 of atmospheric warming ~~.~~ (Haywood et al., 2020; Han et al., 2021). The increase in surface freshwater flux over the Arctic Ocean that is consistent across the PlioMIP2 ensemble can be seen in Figure 6a. The atmospheric freshwater flux is defined as the difference between the precipitation and evaporation (PmE), where a positive PmE means that precipitation exceeds evaporation at the surface. Other possible factors include an increase in runoff due to the reduced Greenland Ice Sheet and a decrease in sea-ice extent in the mid-Pliocene (de Nooijer et al., 2020). ~~In the next subsection, we will~~

355
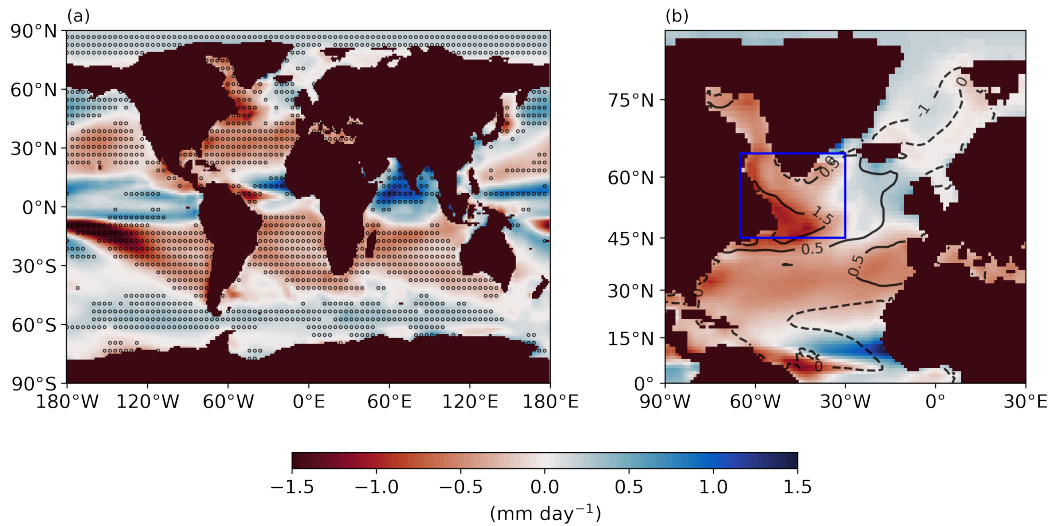
Figure 6. (a) Multi-model mean mPWP-PI difference in surface freshwater flux. Stippling indicates that 12 or more models agree on the sign of the difference. (b) Shading shows the MMM mPWP-PI difference in surface freshwater flux in the North Atlantic. Black contours show the MMM mPWP-PI sea surface salinity anomaly. The approximate extent of the negative PmE anomaly over the Labrador Sea and subpolar North Atlantic is indicated in by the blue box (45-65°N, 30-60°W). A negative PmE anomaly means that evaporation is higher than precipitation.

Changes in the surface freshwater flux in the mid-Pliocene not only affect the Arctic Ocean salinity but also play a considerable role in the strongly increased North Atlantic sea surface salinity. Figure 6b allows us to consider the role ~~of the gateway closure in the freshwater~~ that the atmospheric freshwater flux plays in the increased sea surface salinity in the Labrador Sea and part of the mid-Pliocene subpolar North Atlantic. Shading in Figure 6b shows the MMM PmE anomaly and the sea surface

360 salinity anomaly is indicated by the black contours. We can see here that the surface freshwater flux is decreased over a considerable section of the subpolar North Atlantic despite an increase in MMM precipitation that has been shown in earlier

work (Haywood et al., 2020). Off the coast of Newfoundland, the PmE shading follows sea surface salinity contours quite closely, which is an indication that the sea surface salinity is influenced by changes in surface freshwater flux there.

365 In the next subsection, we will investigate how the mid-Pliocene boundary conditions affect freshwater transport between the Arctic, North Pacific and North Atlantic~~and how this contributes to the changes in~~. Following from that, we will consider the role that the surface freshwater flux and the freshwater transport play in the increase in the Atlantic Ocean sea surface salinity ~~that we observe here~~in the mid-Pliocene.

3.2.2 Freshwater transport

370 In the pre-industrial simulations, freshwater exchange of the Atlantic basin with the Pacific Ocean occurs both at 34°S and through the Bering Strait. The Pacific water that is transported to the Arctic through the Bering Strait is relatively fresh. As the Arctic freshwater is then transported to the Atlantic Ocean via the Canadian Archipelago and Fram Strait into the Labrador and Norwegian Seas, it dampens convection and deep water formation in the high North Atlantic. As mentioned in earlier sections, it has been shown that closing the Bering Strait and Canadian Archipelago decreases the freshwater transport into and

375 out from the Arctic Ocean (Hu et al., 2015; Otto-Bliesner et al., 2017), promoting stronger deep water formation in the North Atlantic. In this section, we will take a closer look at both the freshwater transport through the whole Atlantic basin as well as the exchange of freshwater between the North Pacific and Arctic through the Bering Strait and between the Arctic and North Atlantic via the Fram Strait and Labrador Sea.
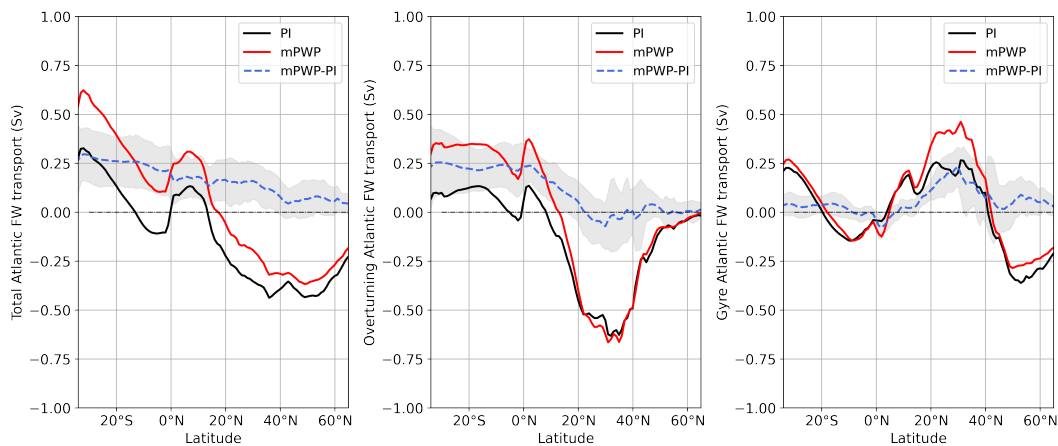
Figure 7. (a) MMM total Atlantic freshwater transport in the mid-Pliocene, pre-industrial and the difference. (b) MMM Atlantic freshwater transport by overturning. (c) MMM Atlantic freshwater transport by wind-driven gyres. The shading indicates one standard deviation of deviation from the MMM difference by individual models, excluding HadGEM3.

380 Figure 7a shows that the MMM southward total freshwater transport into the Atlantic Ocean at 65°N decreases by 0.04 Sv

(-19%) in the mid-Pliocene. This ~~is presumably the main cause of the~~ presumably contributes significantly to the higher MMM sea surface salinity in the North Atlantic shown in Figure 5. At 34°S, the southern boundary of the Atlantic Ocean, the MMM northward transport of freshwater increases by 0.27 Sv (+96%) in the mid-Pliocene. Using Figure 7b and 7c, we can determine whether changes we observe in the total freshwater transport can be attributed to changes in the overturning or gyre circu-lation. Looking at the freshwater imported at the southern Atlantic boundary in Figure 7b and 7c, it is clear that the higher mid-Pliocene import of freshwater at the southern boundary can be attributed almost entirely to the overturning circulation. However, in the North Atlantic the change in Atlantic freshwater transport by overturning is relatively small and inconsis-tent at latitudes higher than 20°N. At latitudes above 20°N, differences in the total Atlantic freshwater transport between the mid-Pliocene and pre-industrial can primarily be linked to the wind-drive gyre circulation, as can be seen in Figure 7c. The freshwater transport by the (northern) subtropical gyre is almost doubled in the mid-Pliocene, while the transport by the sub-polar gyre is decreased at latitudes higher than 50°N.
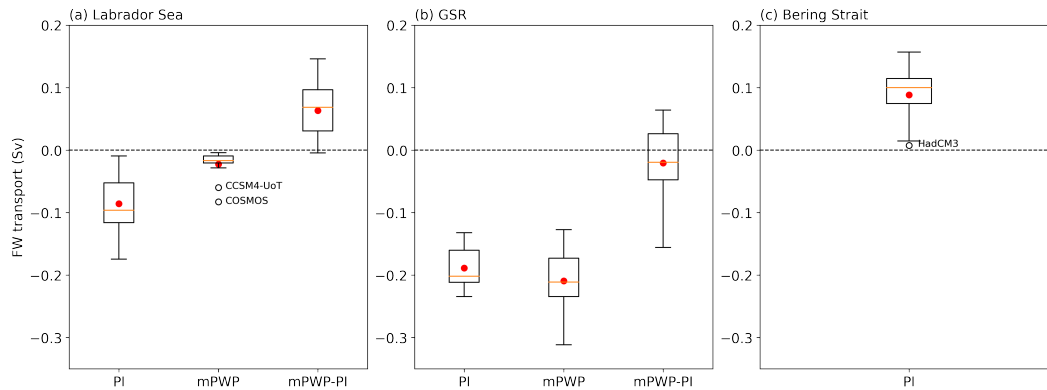
Figure 8. Boxplots of the mean freshwater transport (Sv) in pre-industrial, mid-Pliocene and their difference at 62°N (a) near the northern boundary of the Labrador Sea and (b) across the GSR. (c) Mean freshwater transport (Sv) through the Bering Strait in the pre-industrial. The box covers Q1 (25th percentile) to Q3 (75th percentile), with the median indicated by a horizontal orange line. The whiskers extend from Q1 to Q1-1.5*IQR and from Q3 to Q3+1.5*IQR where IQR=Q3-Q1. A model that falls outside the whiskers is separately shown as an unfilled circle. The MMM is indicated by a red filled circle.

To better understand how the ~~gateway closure impacts~~ mid-Pliocene boundary conditions impact the freshwater transport from the Arctic into the Atlantic Ocean, we differentiate between the total freshwater transport on the western and eastern side of Greenland at 62°N in Figure 8a and 8b. The freshwater transport on the western side of Greenland is entering the Labrador Sea and the transport on the eastern side is going across the Greenland Scotland Ridge (GSR). Note that in the mid-Pliocene, freshwater entering the Labrador Sea from the north cannot originate from the Arctic Ocean and can only result from runoff and the surface freshwater flux into Baffin Bay.

All model simulations show freshwater transport southwards into the Labrador Sea both in the pre-industrial and mid-Pliocene, regardless of an open or closed Canadian Archipelago (see Supplementary Figure S7 for individual model results). However, the MMM freshwater transport into the Labrador Sea (Figure 8a) decreases dramatically with 0.063 Sv (-74%) from the pre-industrial to the mid-Pliocene. We do not observe this decrease in HadGEM3. In Figure 8b, we can see that the MMM freshwater transport increase of 0.021 Sv (+11%) across the GSR in the mid-Pliocene is relatively small and compensates a third of the decrease in freshwater transport into the Labrador Sea. In addition, the box plots indicate that the decrease in freshwater transport into the Labrador Sea is a more consistent feature among the models than the increase of freshwater transport across the GSR. These results are in line with the decrease of the MMM total freshwater transport from the Arctic Ocean to the Atlantic Ocean in the mid-Pliocene (Figure 7a). The decrease in total freshwater transport into the North Atlantic can may partly be explained by the closure of the Bering Strait in the mid-Pliocene, causing a MMM decrease of 0.09 Sv freshwater transport into the Arctic (Figure 8c). It has also previously been shown that closing the Bering Strait leads to less freshwater transported from the Arctic into the North Atlantic (Hu et al., 2015) due to effects on sea-ice motion and freshwater exchange.

While the our results show a robust decrease in freshwater transport plays a crucial role in the increased salinity in the Labrador Sea and subpolar from the Arctic into the North Atlantic, our freshwater transport calculations do not take into account the sea-ice extent and surface freshwater flux also play, which plays an important role in the Arctic freshwater balance (Aagaard and Carmack, 1989). It should be noted that the transport of sea-ice is not included in our freshwater transport calculations. However, all models show a greatly reduced sea-ice cover in the Labrador Sea and Baffin Bay and in most models the annual sea-ice coverage does not extend southwards to 62°N in the mid-Pliocene (Supplementary Figure S8). Therefore, qualitatively, our results will should not be impacted if transport of sea-ice were to be taken into account. The role of changes in

3.2.3 Role of surface freshwater flux and freshwater transport in increased North Atlantic salinity

In the previous subsections we have shown that the increase in North Atlantic sea surface salinity in the mid-Pliocene appears to be linked to changes in both the freshwater transport and the surface freshwater flux is explored further in the next subsection.

3.2.4 Surface freshwater flux

(a) Shading shows the MMM mPWP-PI difference in PmE freshwater flux. Black contours show the MMM mPWP-PI sea surface salinity anomaly. (b) Average mPWP-PI PmE anomaly (40-65°N, 30-70°W) plotted against the mPWP-PI AMOC strength anomaly. The area over which the PmE anomaly is averaged is indicated in (a) by the blue box. A negative PmE anomaly means that the evaporation is higher than precipitation and thus indicates saltening. Figure 6 allows us to consider the role that the atmospheric freshwater flux plays in the increased salinity in the mid-Pliocene North Atlantic. We consider their respective roles in Figure 9. We find a strong and significant correlation ($R = -0.92$, $p < 0.05$) between the mPWP-PI surface freshwater flux anomaly and the sea surface salinity anomaly in the Labrador Sea and eastern subpolar North Atlantic. The atmospheric freshwater flux is defined as the difference between the precipitation and evaporation (PmE), where a positive PmE means that precipitation exceeds evaporation at the surface. Shading in Figure 6a shows the MMM PmE anomaly, with There is

also a moderately strong and significant correlation ($R = -0.53$, $p = 0.04$) between the mPWP-PI freshwater transport through the Bering Strait and the sea surface salinity anomaly~~indicated by the black contours. Off the coast of Newfoundland, the PmE~~

435 ~~shading follows~~, as well as a correlation of similar strength between the mPWP-PI freshwater transport into the Labrador Sea and the sea surface salinity ~~contours quite closely, which is an indication that the sea surface salinity is influenced by changes in freshwater flux there. However, the PmE balance is negative over part of the subpolar North Atlantic experiencing a relatively high~~ anomaly ($R = 0.48$, $p = 0.07$) that falls just outside the 95% confidence level. The freshwater transport across the GSR does not correlate significantly with the North Atlantic sea surface salinity~~increase of 0.6-1.2 psu. When plotting the PmE~~

440 ~~anomaly in the subpolar North Atlantic , averaged over the area indicated by the blue box in Figure 6a , against~~.
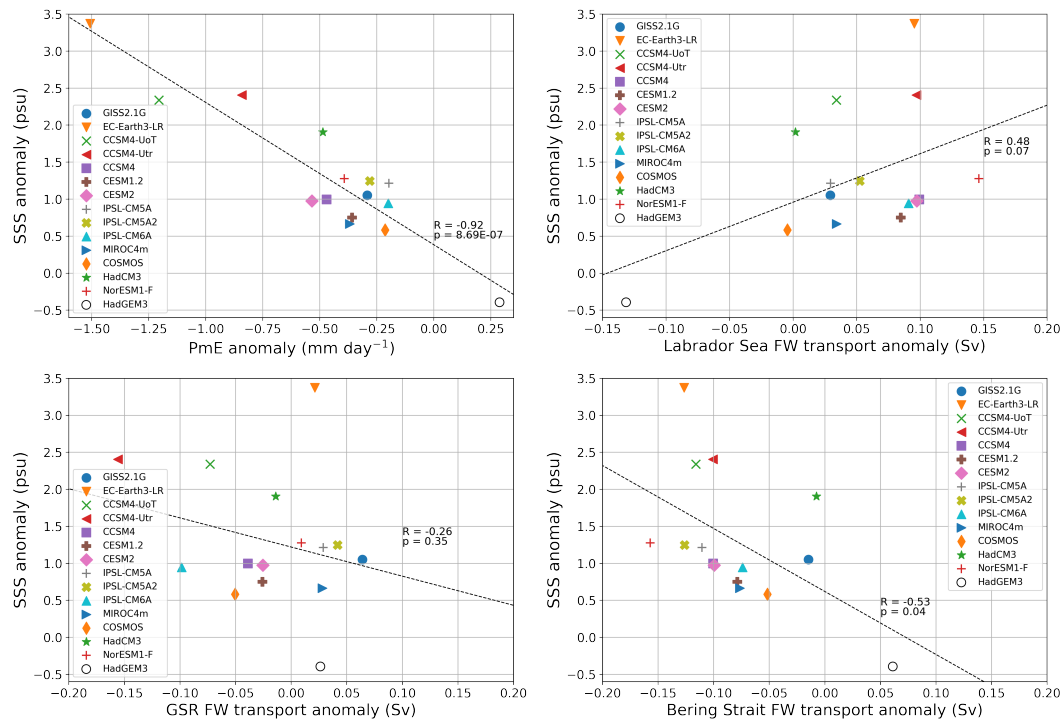
Figure 9. mPWP-PI change in sea surface salinity plotted against (a) the mPWP-PI change in PmE freshwater flux, (b) the mPWP-PI change in northward freshwater transport at the northern boundary of the Labrador Sea (62°N), (c) the mPWP-PI change in northward freshwater transport across the GSR (62°N) and (d) the mPWP-PI change in northward freshwater transport across the Bering Strait. The sea surface salinity and PmE anomalies are averaged over the eastern subpolar North Atlantic and Labrador Sea (45-65°N, 30-60°W); the area indicated by the blue box in Figure 6b.

The results from Figure 9 indicate that there is a link between both the surface freshwater flux and the meridional freshwater transport with the increased North Atlantic salinity but we cannot separate their respective strengths. While Otto-Bliesner et al. (2017) identi decreased freshwater transport due to the closure of Arctic gateways as a mechanism for increasing the AMOC strength~~anomaly~~

445 ~~for individual models in Figure 6b, we find no indication that the PmE freshwater flux is the driving force behind the~~ , our analysis shows that the decreased surface freshwater flux must also play a considerable role. However, the freshwater transport and surface freshwater flux are not independent of each other. Our results point to a complex interplay between different components of the North Atlantic freshwater balance in the mid-Pliocene ~~AMOC strength increase. If this were the case, we would expect a more negative PmE anomaly to correspond to a stronger AMOC, as a negative PmE anomaly would cause~~

450 ~~higher salinity and thus higher ocean water density~~ simulations that combine to result in an increase in North Atlantic salinity and thereby density, ultimately affecting the AMOC strength. As with the sea surface salinity, we see that HadGEM3 does not show the same sign of change in the North Atlantic ~~. Such a trend is not indicated by Figure 6b as linear regression analysis reveals no significant correlation ($R = -0.06$, $p = 0.83$).~~ surface freshwater flux as the rest of the ensemble (Supplementary Figure S9). This further supports that changes in the land-sea mask in the mid-Pliocene play an important role in the change in

455 surface freshwater flux, potentially also linking it to the closure of the Arctic gateways.

3.3 ~~Ocean heat transport~~ Consequences of the stronger AMOC

3.3.1 Ocean heat transport

For all models with an intensified mid-Pliocene AMOC, we would expect the Atlantic OHT in the Northern Hemisphere to

460 also be strengthened in the mid-Pliocene simulations. However, figure 10a shows that while the MMM total Atlantic OHT does increase at some latitudes, this increase is relatively small with a maximum of 0.09 PW (+9%) at 24 °N. Figure 10b and 10c show the relative contributions of the overturning and wind-driven gyre circulation to the MMM OHT. The MMM Atlantic OHT by overturning increases significantly more than the total Atlantic OHT in the NH with a maximum of 0.20 PW (+23%) at 24°N. Between 20-40°N, this increase is robust across the ensemble when considering the standard deviation.

465

While the heat transported by the overturning circulation increases in the mid-Pliocene North Atlantic Ocean, the MMM gyre Atlantic OHT decreases (see figure 10c). This decrease is strongest in the region of the subtropical gyre, with a maximum decrease of -0.12 PW (-15%) at 30°N and a decrease of -0.10 PW (-12%) at 24°N. This suggests that the gyre circulation responds to mid-Pliocene conditions in such a way that it compensates for approximately half of the increase in Atlantic OHT by

470 overturning in the subtropical North Atlantic. When we consider only the latitudes of the subtropical North Atlantic, 20-40°N, we find that the 20-40°N average MMM total Atlantic OHT at these latitudes increases by 0.07 PW (+9%) and the overturning Atlantic OHT increases by more than twice this value: 0.16 PW (+21%).

Figure 11 shows the mPWP-PI change in AMOC strength and total and overturning Atlantic OHT for all models. The OHT

475 is averaged over 20°N-40°N for three reasons: the influence of the overturning circulation on the Atlantic OHT is largest between 20°N-40°N, it is the region where the subtropical gyre also influences the OHT, and most mid-Pliocene simulations show amplified SST warming in the Atlantic Ocean above 40°N. When we compare changes in AMOC strength to those in
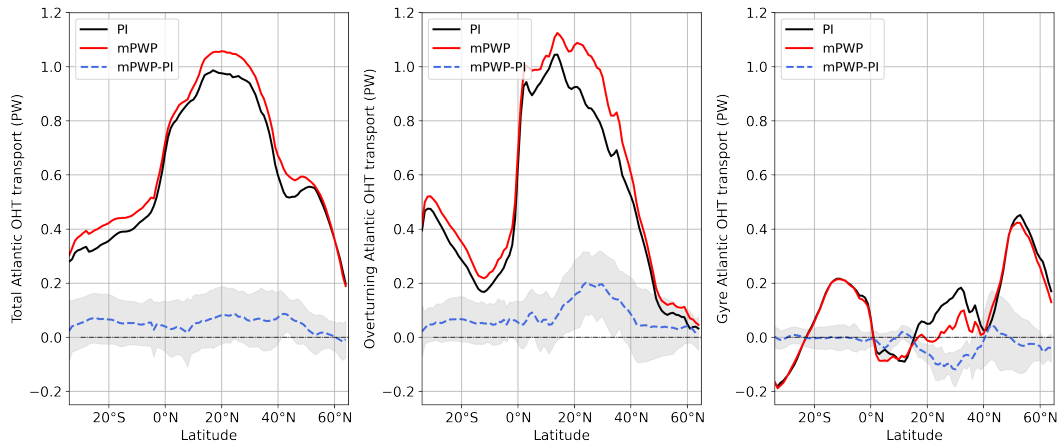
Figure 10. (a) MMM total Atlantic ocean heat transport in the mid-Pliocene, pre-industrial and the difference. (b) MMM Atlantic ocean heat transport by overturning. (c) MMM Atlantic ocean heat transport transport by wind-driven gyres. The shading indicates one standard deviation by individual models from the MMM.
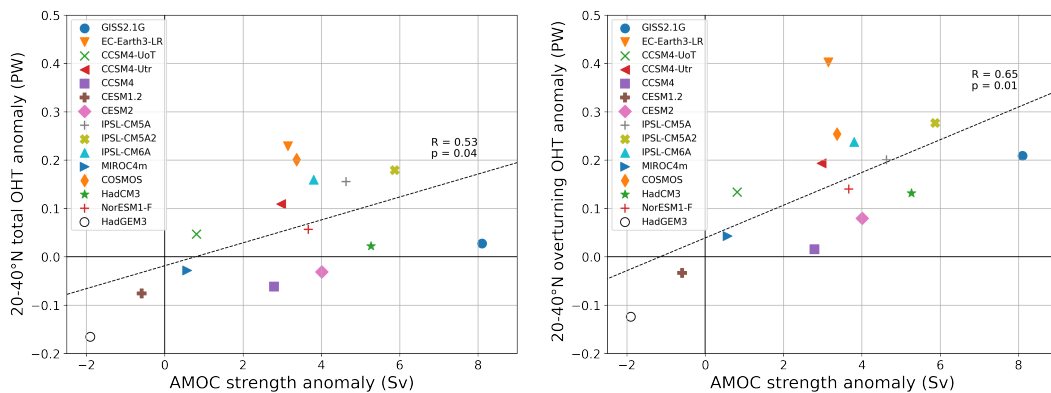
Figure 11. (a) mPWP-PI change in average total Atlantic OHT between 20°N-40°N and change in AMOC strength. (b) mPWP-PI change in overturning Atlantic OHT between 20°N-40°N and change in AMOC strength. Dotted line indicates linear fit by least squares with the ~~slope~~ correlation coefficient R and ~~R^2~~ p-value of fit shown.

the total OHT, not all models show that a stronger AMOC is accompanied by a higher total Atlantic OHT. However, when considering the OHT by overturning, all models with an intensified mid-Pliocene AMOC also have enhanced Atlantic OHT by overturning. A linear least-squares regression performed on the AMOC and overturning OHT reveals a slope that is 42% higher than slope of the regression between the AMOC and total OHT, as well as a better fit indicated by a higher R^2 and substantially lower p-value. This result indicates that OHT components should be considered separately when looking at the response of the Atlantic OHT to a stronger mid-Pliocene AMOC.

Table 2. Results of least square linear fit between the total or overturning OHT mPWP-PI anomaly with the AMOC strength anomaly. The latitude range indicates over what latitudes the OHT has been averaged.

	OHT component	Latitude range OHT	Slope (PW/Sv)	Intercept (PW)	R^2	P-value
All models	Total	20°N-40°N	~~0.023~~ 0.024	-0.019	~~0.28~~ 0.53	0.044
	Overturning	20°N-40°N	0.034	~~0.040~~ 0.039	~~0.42~~ 0.65	0.009
	Total	30°S-60°N	0.018	-0.014	~~0.25~~ 0.50	0.056
	Overturning	30°S-60°N	0.021	0.006	~~0.33~~ 0.58	0.025
All models excluding EC-Earth3-LR	Total	20°N-40°N	0.024	-0.031	~~0.33~~ 0.58	0.031
	Overturning	20°N-40°N	0.034	0.021	~~0.59~~ 0.77	0.001
	Total	30°S-60°N	0.018	-0.023	~~0.29~~ 0.54	0.045
	Overturning	30°S-60°N	0.020	-0.006	~~0.47~~ 0.69	0.006

In Table 2, the results of least-square linear fits between the total OHT and the AMOC strength and the overturning OHT and the AMOC strength are shown for different latitude ranges over which the OHT is averaged. When considering the majority of the Atlantic Ocean basin (30°S-60°N), the regression shows an increased slope and R^2 value when performing it on the overturning OHT component rather than on the total OHT. We have performed the regressions also when excluding EC-Earth3-LR, which is an outlier in Figure 10a and 10b due to its exceptionally large OHT increase. When EC-Earth3-LR is excluded, the R^2 increases significantly for all cases, especially for the regression with the overturning OHT, without substantial changes in the slope. In addition, the y-intercept is closer to zero and the p-value decreases dramatically for the overturning OHT. Overall, these results suggest that the overturning OHT is a better indicator of the direct response of the OHT to a stronger AMOC in the mid-Pliocene. Overall, the PlioMIP2 ensemble shows a rather consistent response in the Atlantic OHT associated with overturning, where a stronger AMOC leads to enhanced Atlantic OHT by overturning.

3.4 ~~Transports by the subtropical gyre~~

3.3.1 Transports by the subtropical gyre

Figure 10c showed that the MMM Atlantic OHT by the wind-driven gyre circulation shows a substantial decrease in the (northern) subtropical gyre region. At the same time, the MMM Atlantic freshwater transport of the northern subtropical gyre is almost doubled in the mid-Pliocene (Figure 7c), meaning that less salt is being transported northwards by the subtropical gyre circulation. One possibility is that the subtropical gyre circulation itself responds to mid-Pliocene conditions through its coupling to the atmosphere. As wind stress fields are not available for the entire PlioMIP2 ensemble, we investigate changes in surface winds that drive the gyre circulation in Figure 12. Figure 12a shows the zonal mean curl of the MMM wind velocity at 1000 hPa in the North Atlantic. A positive wind velocity curl is associated with counterclockwise motion, the subpolar gyre, and a negative wind velocity curl with clockwise motion, the subtropical gyre. The wind velocity curl in the subpolar region
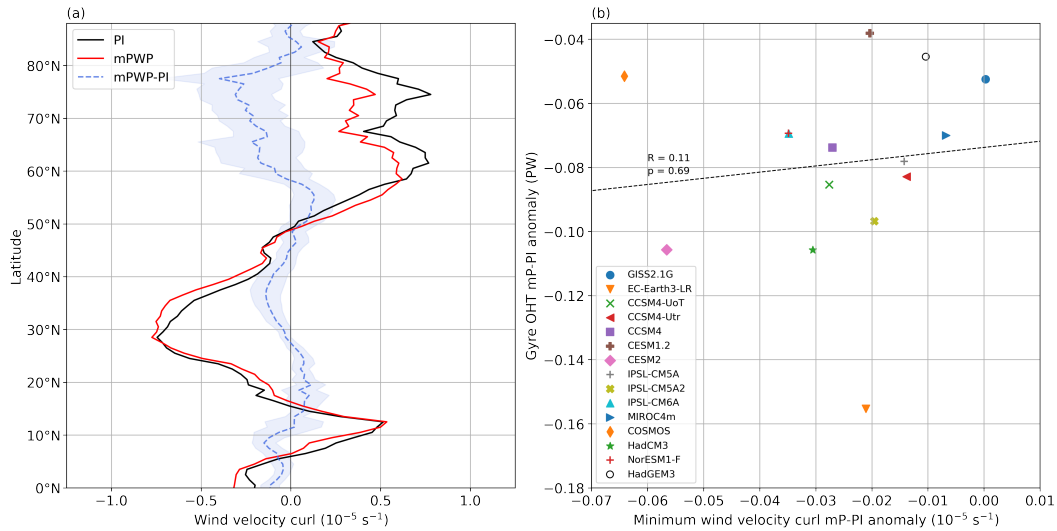
Figure 12. (a) MMM Atlantic zonal mean 1000 hPa wind velocity curl ($\frac{dv}{dx} - \frac{du}{dy}$) in the pre-industrial and mid-Pliocene, and their difference. Shading indicates one standard deviation from the MMM difference by individual models. (b) The minimum zonal mean 1000 hPa wind velocity curl between 20-40°N plotted against the 20-40°N average OHT gyre component anomaly for individual models.

shows a substantial decrease, indicating weakening of the subpolar gyre circulation. In the subtropical gyre region, there is a shift in the wind velocity curl minimum towards higher latitudes but we do not see a significant change in magnitude of the MMM zonal mean wind velocity curl. This result indicates that there are no substantial changes in the mid-Pliocene wind circulation driving the subtropical gyre, and thus not in the subtropical gyre circulation itself. The lack of change in the subtropical gyre circulation is confirmed by the upper 500 m ocean meridional velocity, averaged over the 20-40°N latitude band, which is similar in the mid-Pliocene and pre-industrial outside of the highly variable Gulf Stream region (Supplementary Figure S10). Figure 12b also does not suggest a connection between changes in the surface winds and the OHT by the subtropical gyre. No consistent relationship can be found between the minimum wind velocity curl in the subtropical gyre region and Atlantic OHT by the subtropical gyre when performing a least-squares linear regression ($R = 0.11$, $p = 0.69$). Therefore, we do not see any changes in the subtropical gyre circulation that could explain the substantial decrease in OHT by the gyre between 20-40°N.

Without substantial changes to the wind-driven gyre circulation itself, changes in OHT and freshwater transport by the subtropical gyre may be linked to zonal asymmetry in the mPWP-PI anomalies in temperature and salinity. A zonal asymmetry in temperature or salinity could lead to more transport on the eastern or western part of the Atlantic basin, influencing the total gyre transport. Figure 13a and Figure 13b show the difference between mid-Pliocene and pre-industrial SST and SSS respectively for the subtropical gyre region. A zonal asymmetry can be seen in both fields, with the eastern Atlantic becoming relatively warmer and saltier than the western Atlantic in the mid-Pliocene. When taking the meridional average over 20-40°N for the SST and SSS, we find a zonal gradient in SST and SSS anomalies in Figure 13c and Figure 13d. For each model, the
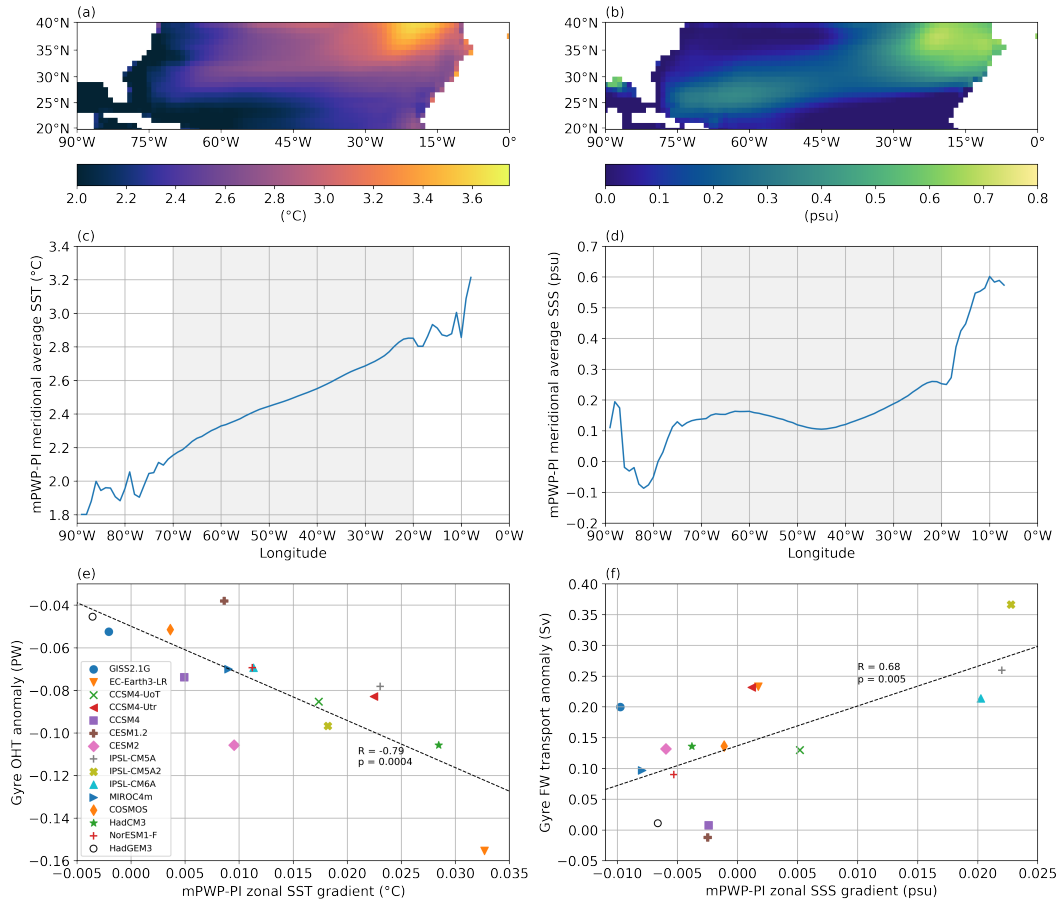
Figure 13. (a) MMM mPWP-PI Atlantic SST difference between 20-40°N. (b) MMM mPWP-PI Atlantic SSS difference between 20-40°N. (c) MMM meridional mean mPWP-PI Atlantic SST difference between 20-40°N. (d) MMM meridional mean mPWP-PI Atlantic SSS difference between 20-40°N. (e) Individual model mPWP-PI mean difference in zonal SST gradient from (c) between 20-70°W plotted against the mPWP-PI difference in OHT gyre component. (f) Individual model mPWP-PI mean difference in zonal SSS gradient from (d) between 20-70°W plotted against the mPWP-PI difference of the gyre freshwater transport.

change in zonal SST gradient averaged between -20 and -70°E (shaded grey in Figure 13c) is plotted against the Atlantic gyre OHT anomaly in Figure 13e. This reveals a significant negative correlation ($R = -0.79$, $p < 0.05$) meaning that a larger zonal

525   gradient in SST anomalies corresponds to a larger decrease in OHT by the gyre. The same plot is shown for the average zonal gradient in the SSS anomalies and the Atlantic gyre freshwater transport in Figure 13f. While the relationship is less robust than that between the SST gradient and OHT, a significant positive correlation ($R = 0.66$, $p < 0.05$) is found where a larger gradient in SSS anomalies is related to more northward freshwater transport by the subtropical gyre.

4 Discussion

530 While there is no consistent relationship between the AMOC strength and average North Atlantic SST warming (Zhang et al., 2021b), the correlation maps (Figure 3 and Supplementary Figure S2) illustrate that a stronger mid-Pliocene AMOC exerts a relatively larger influence on North Atlantic SSTs. A subset of the models does not show an increase in correlation in the mid-Pliocene: CCSM4, CESM1.2, CESM2, IPSL-CM6A and HadGEM3. As HadGEM3 uses the same land-sea mask in their mid-Pliocene simulations, the lack of stronger correlation is expected for this model. For the other models, the reason is not

535 so evident. Three out of these four models, CCSM4, CESM1.2 and CESM2, come from the same model family. CCSM4 and CESM2 also show a relatively small increase in overturning OHT with a stronger mid-Pliocene AMOC compared to the other models, even though their sea surface salinity and gateway transport are in line with ensemble behavior.

The high correlation found between North Atlantic SSTs and the AMOC strength in the mid-Pliocene suggests that there

540 likely is a relationship between the stronger AMOC and the amplified North Atlantic SST warming in the mid-Pliocene in the PlioMIP2 ensemble. However, the effect of the AMOC on North Atlantic SSTs is strongly model dependent and cannot be simply quantified. Other important factors that may influence the SSTs are atmospheric processes and the presence of sea-ice (Zhang et al., 2019), as well as model dynamics. For instance, enhanced vertical mixing has been shown to promote surface temperature anomalies at high latitudes in the Pliocene (Lohmann et al., 2022). These factors vary among the different models

545 (e.g. Supplementary Figure S8) and cause a varied response of North Atlantic SSTs to mid-Pliocene boundary conditions and CO_2 increase. However, Burton et al. (in prep.) show that North Atlantic SSTs in the mid-Pliocene are predominantly driven by changes in geography and ice sheets. As we have shown that the mid-Pliocene AMOC strengthens ~~as a result of~~ is related to these boundary conditions, specifically the closure of the Arctic gateways, the amplified warming of North Atlantic SSTs and the intensified AMOC are related.

550

When considering proxy SST data in the North Atlantic, sites 609, 982, 642 and 907 are specifically of interest as they are closest to above-average MMM SST warming in the North Atlantic (Figure 2b). Disregarding HadGEM3, there are four models at these sites that consistently show the highest warming: EC-Earth3-LR, CCSM4-Utr, CCSM4-UoT and CESM2 (Figure 2c). While these models all have a stronger mid-Pliocene AMOC, they do not have another common factor that directly connects

555 this warming to a stronger mid-Pliocene AMOC, such as a large increase in overturning or total OHT or a strong correlation of the AMOC to North Atlantic SSTs. It has however been shown by Haywood et al. (2020) that these four models have the highest Earth system sensitivity (ESS) of the PlioMIP2 ensemble together with CESM1.2. On the other hand, their equilibrium climate sensitivities (ECS) vary, where only CESM2 and CESM1.2 are among the highest in the ensemble. As the ESS takes into account long-term feedbacks from ice sheets and paleogeographic boundary conditions, the relatively high warming in

560 these models, which aligns with the warm reconstructed SSTs at site 962 and 942, may be related to these feedbacks. This strengthens the argument that the AMOC likely does play a role in the amplified North Atlantic warming, as the ~~stronger AMOC is a direct consequence of~~ strengthening of the mid-Pliocene AMOC is related to the boundary conditions. HadGEM3

showing high warming at sites 642 and 907 is probably related to the fact that its ECS of 5.55°C (Andrews et al., 2019) is the highest of all PlioMIP2 models. Note that HadGEM3 is not among the warmest models at sites 609 and 982, which we expect

565 are the sites that are impacted most by increased OHT due to a stronger mid-Pliocene AMOC.

The AMOC becomes stronger in almost all mid-Pliocene simulations, despite the above-average warming in the subpolar North Atlantic. In future simulations, ocean warming often leads to a weakening AMOC by inhibiting deepwater formation. In our results we show that the strengthening of the AMOC in the mid-Pliocene is a result of high salinity in the Labrador Sea

570 and subpolar North Atlantic. The high salinity is principally caused by two factors: a decreased freshwater transport into the Labrador Sea due to the closure of the Canadian Archipelago . While our results show that a negative Atlantic PmE anomaly plays a role by possibly amplifying the increase in salinity in the mid-Pliocene, they do not suggest that the PmE anomaly is the main cause of the high salinity driving the stronger mid-Pliocene AMOCand a decrease in surface freshwater flux. Another factor in the increased salinity could be the absence of sea-ice over the Labrador Sea in the mid-Pliocene (Supplementary

575 Figure S8). However, we find that the annual sea-ice cover does not extend into the Labrador Sea in the pre-industrial for the majority of the models. In addition, the high salinity persists below the sea surface as shown by the average top 100 m salinity (Supplementary Figure S6). This field shows the same pattern as the sea surface salinity and its mPWP-PI anomaly is of comparable magnitude. Overall, these our results support that the high mid-Pliocene (sea surface) salinity in the Labrador Sea and subpolar North Atlantic is a result of related to the closure of the Bering Strait and Canadian Archipelago, both through the

580 freshwater transport as well as through effects on the surface freshwater flux.

The model response of the total Atlantic ocean heat transport (OHT) to a stronger mid-Pliocene AMOC is diverse: not all PlioMIP2 models that simulate an intensified AMOC also show enhanced Atlantic OHT in the mid-Pliocene. The opposing response of OHT by overturning and OHT by the gyre in the subtropical gyre region is very likely to be an important cause

585 of this diversity, where individual model dynamics govern the degree to which the two components compensate each other's increase or decrease. However, when considering the overturning component only, all of the models that have a stronger mid-Pliocene AMOC show stronger associated OHT.

We expected It appears that the opposing response of the subtropical gyre OHT component would does not result from coupling

590 between the atmospheric forcing of the gyre circulation and the atmosphere. In that case, an increase in AMOC strength would lead to increased Atlantic OHT by overturning between 20°N-40°N. This higher OHT by overturning decreases the meridional temperature gradient between these latitudes in the ocean and thereby also at the surface. A decrease in surface winds due to the reduced meridional temperature gradient at the surface would induce a weakening in the subtropical gyre circulation and thus a decrease in strength of the Atlantic OHT gyre component. While this seems to be a plausible mechanism for explaining

595 the opposite behavior of the overturning and gyre OHT component, our results do not show that this mechanism plays role in the response of the PlioMIP2 ensemble as over the mid-Pliocene Atlantic Ocean. Such a mechanism has been proposed by earlier studies such as Farneti and Vallis (2013). As there are no substantial changes in the gyre circulation itself. It appears

that changes in the ~~that changes in the~~ , we find that the (zonal) changes in ocean temperature and salinity fields are responsible for altering the OHT and freshwater transport by the subtropical gyre. We observe that between 20°N and 40°N, the eastern part of the Atlantic basin becomes relatively warmer and saltier than the western part in the mid-Pliocene. This results in the gyre circulation transporting relatively more heat and salt southwards than in the pre-industrial. The relatively high temperature and salinity in the eastern subtropical North Atlantic appears to originate from the even warmer and saltier mid-Pliocene subpolar North Atlantic, features that we have related to the stronger AMOC and Arctic gateway closure, respectively. The warm and salty water in the subpolar North Atlantic is transported eastwards by the northern branch of the subtropical gyre and subsequently transported southwards, resulting in the zonal asymmetry we observe. It is possible that the weakened subpolar gyre circulation plays a role in increased eastward transport of the warm and salty subpolar North Atlantic water.

Our results point to a mechanism of compensation between the OHT components in the subtropical gyre region in the Atlantic Ocean. This compensation is, however, not via the atmosphere as has been suggested previously to be the case in the pre-industrial (Vallis and Farneti, 2009; Farneti and Vallis, 2013). Rather, our results for the mid-Pliocene indicate that the enhanced warming in the mid-Pliocene subpolar North Atlantic SSTs causes more eastward and subsequent southward heat transport by the subtropical gyre. This suggests that the mid-Pliocene background state may affect OHT dynamics, and thereby highlights potential differences between the mid-Pliocene and near-future climate. We do not observe such a compensating mechanism in the overturning and gyre components of the freshwater transport.

5 Conclusions

In our study, we have employed fifteen models from the PlioMIP2 ensemble to investigate what drives the stronger AMOC in the mid-Pliocene simulations and how the Atlantic OHT and North Atlantic SSTs respond to this strengthening. All models that simulate a stronger mid-Pliocene AMOC show that the closure of the Bering Strait and Canadian Archipelago in the mid-Pliocene leads to a dramatic decrease in southward freshwater transport into the Labrador Sea. The ~~ensuing~~ increased salinity in the Labrador Sea and subpolar North Atlantic, which is related to both the decreased freshwater transport through the Canadian Archipelago and decreased surface freshwater flux over the subpolar North Atlantic, stimulates deepwater formation in these areas, leading to a stronger AMOC. These results ~~agree~~ are consistent with the conclusions of Otto-Bliesner et al. (2017), who showed that closing the Bering Strait and Canadian Archipelago in their CCSM4 model led to a stronger mid-Pliocene AMOC due to altered freshwater transport in the Arctic and North Atlantic. We have shown in this study that ~~this~~ the increase in salinity in the high North Atlantic is a consistent ~~response to the closure of these Arctic gateways across the~~ feature across the mid-Pliocene simulations in the PlioMIP2 ensemble and ~~is thereby the driver of the reported stronger AMOC in the~~ can be confidently linked to the stronger mid-Pliocene ~~simulations~~AMOC.

We show that the response of the total Atlantic OHT to a stronger mid-Pliocene AMOC seems inconsistent among models due to a compensation mechanism between the overturning circulation and wind-driven gyre circulation. When separating the

OHT into two components, one driven by the overturning circulation and the other by the wind-driven gyre circulation, we find that the OHT associated with overturning does consistently increase with a stronger AMOC. The OHT associated with the subtropical gyre decreases as a response to ocean temperatures increasing more in the east than in the west of the North Atlantic in the mid-Pliocene. This decrease in gyre OHT partially compensates the higher OHT by overturning in the northern

635 subtropical gyre region. As individual model dynamics are highly variable, the degree of compensation differs among models. However, the mean response is consistent. We argue that the OHT components should be considered separately when evaluating the response of the OHT to a stronger mid-Pliocene AMOC. When doing so, we find that the stronger mid-Pliocene AMOC in the PlioMIP2 ensemble does lead to enhanced Atlantic OHT by the overturning circulation.

640 It has been suggested that the ~~decrease in~~ improved data-model ~~mismatch~~ agreement in the North Atlantic may be due to a stronger AMOC transporting more heat to the North Atlantic in the PlioMIP2 ensemble (Haywood et al., 2020). Indeed, our results show that the AMOC has a stronger influence on North Atlantic SSTs in the mid-Pliocene than in the pre-industrial. However, the spatial extent and magnitude of this effect is highly variable among individual models, which may explain why Zhang et al. (2021b) were not able to identify a consistent relationship between the AMOC strength and average North Atlantic

645 SST warming. It remains difficult to quantify the extent of the influence of the AMOC on North Atlantic SSTs, but our study shows that its influence is significant. Furthermore, we conclude that the AMOC is an important factor in explaining the better agreement of the PlioMIP2 ensemble SSTs with reconstructions in the North Atlantic.

The results presented in this study provide an in-depth look at how the stronger mid-Pliocene AMOC in PlioMIP2 is driven

650 and what its consequences are for the OHT and SST warming in the North Atlantic. They also raise further questions, such as the degree to which the decrease in OHT by the gyre circulation is a response to the increase in OHT by the stronger Atlantic overturning circulation and how the ECS and ESS of individual models may influence modelled SST warming in the mid-Pliocene. Furthermore, given the influence of the stronger mid-Pliocene AMOC on the Atlantic OHT and enhanced SST warming, it raises the question as to what extent and in which context the mid-Pliocene is suitable as a future climate analog.

655 The impact of a stronger AMOC on the regional and global climate is significant, and must be taken into consideration when comparing the mid-Pliocene climate to future warming scenarios.

Code and data availability. PlioMIP2 data used for this paper is available upon request from Alan M. Haywood (a.m.haywood@leeds.ac.uk), with the exception of IPSL-CM6A, EC-Earth3-LR and GISS2.1G. PlioMIP2 data from IPSL-CM6A, EC-Earth3-LR and GISS2.1G can be obtained from the Earth System Grid Federation (ESGF) (https://esgf-node.llnl.gov/search/cmip6/, last access: 14 February 2022). The $U_{37}^{k'}$

660 and Mg/Ca SST reconstructions from McClymont et al. (2020) can be obtained through https://doi.pangaea.de/10.1594/PANGAEA.911847 (last access: 24 January 2022) and the $U_{37}^{k'}$ SST reconstructions from Foley and Dowsett (2019) can be obtained through https://doi.org/10.5066/P9YP3DTV (last access: 24 January 2022). The observational pre-industrial SSTs from the NOAA ERSST5 dataset (Huang et al., 2017) can be downloade from https://www.ncei.noaa.gov/products/extended-reconstructed-sst (last access: 24 January 2022).

665   The Jupyter Notebooks used for data processing and analysis are available through Zenodo: https://doi.org/10.5281/zenodo.7288756 (Weiffenbach, 2022).

Author contributions. JEW, MLJB, HAD and ASvdH designed the work. JEW performed the analysis and wrote the manuscript of the paper. The remaining authors provided the PlioMIP2 experiments and contributed to the discussion of the results and the contents of the manuscript.

Competing interests. The authors declare that they have no conflict of interest.

670   *Acknowledgements.* We thank the two anonymous reviewers for their constructive feedback and suggestions.

The work by Julia E. Weiffenbach, Michiel L. J. Baatsen, Henk A. Dijkstra and Anna S. von der Heydt was carried out under the program of the Netherlands Earth System Science Centre (NESSC), financially supported by the Ministry of Education, Culture and Science (OCW grant number 024.002.001)). CCSM4-Utr simulations were performed at the SURFsara Dutch national computing facilities and were
675   sponsored by NWO-EW (Netherlands Organisation for Scientific Research, Exact Sciences) under the projects 17189 and 2020.022.

Bette L. Otto-Bliesner, Esther C. Brady and Ran Feng acknowledge support from U.S. National Science Foundation grant numbers 1814029, and 1852977 (B.L.O and E.C.B). The CCSM4 and CESM1 and CESM2 simulations are performed with high-performance computing support from Cheyenne (doi:10.5065/D6RX99HX) provided by NCAR's Computational and Information Systems Laboratory, sponsored by the
680   National Science Foundation.

Alan M. Haywood and Julia C. Tindall acknowledge the FP7 Ideas programme from the European Research Council (grant no. PLIO-ESS, 278636), the Past Earth Network (EPSRC grant no. EP/M008.363/1) and the University of Leeds Advanced Research Computing service. Julia C. Tindall was also supported through the Centre for Environmental Modelling and Computation (CEMAC), University of Leeds.
685
Christian Stepanek acknowledges funding from the Helmholtz Climate Initiative REKLIM. Christian Stepanek and Gerrit Lohmann acknowledge funding via the Alfred Wegener Institute's research programme Marine, Coastal and Polar Systems.

W. Richard Peltier and Deepak Chandan were supported by Canadian NSERC Discovery Grant A9627, and they wish to acknowledge
690   the support of SciNet HPC Consortium for providing computing facilities. SciNet is funded by the Canada Foundation for Innovation under the auspices of Compute Canada, the Government of Ontario, the Ontario Research Fund – Research Excellence, and the University of Toronto.

Zhongshi Zhang and Xiangyu Li acknowledge financial support from the National Natural Science Foundation of China (grant no. 42005042),
695   the China Scholarship Council (201804910023) and the China Postdoctoral Science Foundation (project no. 2015M581154). The NorESM

simulations benefitted from resources provided by UNINETT Sigma2 – the National Infrastructure for High Performance Computing and Data Storage in Norway.

Charles J. R. Williams and Dan Lunt acknowledge the financial support of the UK Natural Environment Research Council (NERC)-funded
700   SWEET project (research grant no. NE/P01903X/1), as well as the European Research Council under the European Union's Seventh Framework Programme (FP/2007-868 2013) (ERC grant agreement no. 340923).

PlioMIP simulations with GISS2.1G were made possible by the NASA High-End Computing (HEC) Program through the NASA Center for Climate Simulation (NCCS) at Goddard Space Flight Center.
705

Ning Tan, Camille Contoux and Gilles Ramstein were granted access to the HPC resources of TGCC under the allocations 2016-A0030107732, 2017-R0040110492 and 2018-R0040110492 (gencmip6) and 2019-A0050102212 (gen2212) provided by GENCI. The IPSL-CM6 team of the IPSL Climate Modelling Centre (https://cmc.ipsl.fr/, last access: 28 April 2021) is acknowledged for having developed, tested, evaluated and tuned the IPSL climate model, as well as having performed and published the CMIP6 experiments.
710

Qiong Zhang acknowledges support from the Swedish Research Council (2013-06476 and 2017-04232). The EC-Earth3-LR simulations were performed on resources provided by the Swedish National Infrastructure for Computing (SNIC) at the National Supercomputer Centre (NSC) partially funded by the Swedish Research Council through grant No. 2018-05913.

715   Wing-Le Chan and Ayao Abe-Ouchi acknowledge funding from JSPS KAKENHI (Grant no. 17H06104) and MEXT KAKENHI (Grant no. 17H06323), and are grateful to JAMSTEC for use of the Earth Simulator.

References

Aagaard, K. and Carmack, E. C.: The role of sea ice and other fresh water in the Arctic circulation, Journal of Geophysical Research, 94, 14 485, https://doi.org/10.1029/JC094iC10p14485, 1989.

Andrews, T., Andrews, M. B., Bodas-Salcedo, A., Jones, G. S., Kuhlbrodt, T., Manners, J., Menary, M. B., Ridley, J., Ringer, M. A., Sellar, A. A., Senior, C. A., and Tang, Y.: Forcings, Feedbacks, and Climate Sensitivity in HadGEM3-GC3.1 and UKESM1, Journal of Advances in Modeling Earth Systems, 11, 4377–4394, https://doi.org/10.1029/2019MS001866, 2019.

Ba, J., Keenlyside, N. S., Latif, M., Park, W., Ding, H., Lohmann, K., Mignot, J., Menary, M., Otterå, O. H., Wouters, B., and others: A multi-model comparison of Atlantic multidecadal variability, Climate dynamics, 43, 2333–2348, https://doi.org/10.1007/s00382-014-2056-1, 2014.

Baatsen, M. L. J., von der Heydt, A. S., Kliphuis, M. A., Oldeman, A. M., and Weiffenbach, J. E.: Warm mid-Pliocene conditions without high climate sensitivity: the CCSM4-Utrecht (CESM 1.0.5) contribution to the PlioMIP2, Climate of the Past, https://doi.org/10.5194/cp-2021-140, 2022.

Badger, M. P. S., Schmidt, D. N., Mackensen, A., and Pancost, R. D.: High-resolution alkenone palaeobarometry indicates relatively stable pCO$_2$ during the Pliocene (3.3–2.8 Ma), Philosophical Transactions of the Royal Society A: Mathematical, Physical and Engineering Sciences, 371, 20130 094, https://doi.org/10.1098/rsta.2013.0094, 2013.

Booth, B. B., Dunstone, N. J., Halloran, P. R., Andrews, T., and Bellouin, N.: Aerosols implicated as a prime driver of twentieth-century North Atlantic climate variability, Nature, 484, 228–232, https://doi.org/10.1038/nature10946, 2012.

Bryan, F. O., Hecht, M. W., and Smith, R. D.: Resolution convergence and sensitivity studies with North Atlantic circulation models. Part I: The western boundary current system, Ocean Modelling, 16, 141–159, https://doi.org/10.1016/j.ocemod.2006.08.005, 2007.

Bryan, K.: Seasonal variation in meridional overturning and poleward heat transport in the Atlantic and Pacific Oceans: A model study, J. Mar. Res, 40, 39–53, 1982.

Burke, K. D., Williams, J. W., Chandler, M. A., Haywood, A. M., Lunt, D. J., and Otto-Bliesner, B. L.: Pliocene and Eocene provide best analogs for near-future climates, Proceedings of the National Academy of Sciences, 115, 13 288–13 293, https://doi.org/10.1073/pnas.1809600115, 2018.

Chan, W.-L. and Abe-Ouchi, A.: Pliocene Model Intercomparison Project (PlioMIP2) simulations using the Model for Interdisciplinary Research on Climate (MIROC4m), Climate of the Past, 16, 1523–1545, https://doi.org/10.5194/cp-16-1523-2020, 2020.

Chandan, D. and Peltier, W. R.: Regional and global climate for the mid-Pliocene using the University of Toronto version of CCSM4 and PlioMIP2 boundary conditions, Climate of the Past, 13, 919–942, https://doi.org/10.5194/cp-13-919-2017, 2017.

Clement, A., Bellomo, K., Murphy, L. N., Cane, M. A., Mauritsen, T., Rädel, G., and Stevens, B.: The Atlantic Multidecadal Oscillation without a role for ocean circulation, Science, 350, 320–324, https://doi.org/10.1126/science.aab3980, 2015.

de Boer, A. M., Gnanadesikan, A., Edwards, N. R., and Watson, A. J.: Meridional Density Gradients Do Not Control the Atlantic Overturning Circulation, Journal of Physical Oceanography, 40, 368–380, https://doi.org/10.1175/2009JPO4200.1, 2010.

de la Vega, E., Chalk, T. B., Wilson, P. A., Bysani, R. P., and Foster, G. L.: Atmospheric CO2 during the Mid-Piacenzian Warm Period and the M2 glaciation, Scientific Reports, 10, 11 002, https://doi.org/10.1038/s41598-020-67154-8, 2020.

de Nooijer, W., Zhang, Q., Li, Q., Zhang, Q., Li, X., Zhang, Z., Guo, C., Nisancioglu, K. H., Haywood, A. M., Tindall, J. C., Hunter, S. J., Dowsett, H. J., Stepanek, C., Lohmann, G., Otto-Bliesner, B. L., Feng, R., Sohl, L. E., Chandler, M. A., Tan, N., Contoux, C., Ramstein, G., Baatsen, M. L. J., von der Heydt, A. S., Chandan, D., Peltier, W. R., Abe-Ouchi, A., Chan, W.-L., Kamae, Y., and Brierley, C. M.:

755   Evaluation of Arctic warming in mid-Pliocene climate simulations, Climate of the Past, 16, 2325–2341, https://doi.org/10.5194/cp-16-2325-2020, 2020.

Dijkstra, H. A.: Characterization of the multiple equilibria regime in a global ocean model, Tellus A: Dynamic Meteorology and Oceanography, 59, 695–705, https://doi.org/10.1111/j.1600-0870.2007.00267.x, 2007.

Dowsett, H., Dolan, A., Rowley, D., Moucha, R., Forte, A. M., Mitrovica, J. X., Pound, M., Salzmann, U., Robinson, M., Chandler, M.,
760   Foley, K., and Haywood, A.: The PRISM4 (mid-Piacenzian) paleoenvironmental reconstruction, Climate of the Past, 12, 1519–1538, https://doi.org/10.5194/cp-12-1519-2016, 2016.

Dowsett, H. J., Cronin, T. M., Poore, R. Z., Thompson, R. S., Whatley, R. C., and Wood, A. M.: Micropaleontological Evidence for Increased Meridional Heat Transport in the North Atlantic Ocean During the Pliocene, Science, 258, 1133–1135, https://doi.org/10.1126/science.258.5085.1133, 1992.

765   Dowsett, H. J., Foley, K. M., Stoll, D. K., Chandler, M. A., Sohl, L. E., Bentsen, M., Otto-Bliesner, B. L., Bragg, F. J., Chan, W.-L., Contoux, C., Dolan, A. M., Haywood, A. M., Jonas, J. A., Jost, A., Kamae, Y., Lohmann, G., Lunt, D. J., Nisancioglu, K. H., Abe-Ouchi, A., Ramstein, G., Riesselman, C. R., Robinson, M. M., Rosenbloom, N. A., Salzmann, U., Stepanek, C., Strother, S. L., Ueda, H., Yan, Q., and Zhang, Z.: Sea Surface Temperature of the mid-Piacenzian Ocean: A Data-Model Comparison, Scientific Reports, 3, 2013, https://doi.org/10.1038/srep02013, 2013.

770   Farneti, R. and Vallis, G. K.: Meridional Energy Transport in the Coupled Atmosphere–Ocean System: Compensation and Partitioning, Journal of Climate, 26, 7151–7166, https://doi.org/10.1175/JCLI-D-12-00133.1, 2013.

Feng, R., Otto-Bliesner, B. L., Xu, Y., Brady, E., Fletcher, T., and Ballantyne, A.: Contributions of aerosol-cloud interactions to mid-Piacenzian seasonally sea ice-free Arctic Ocean, Geophysical Research Letters, 46, 9920–9929, https://doi.org/10.1029/2019GL083960, 2019.

775   Feng, R., Otto-Bliesner, B. L., Brady, E. C., and Rosenbloom, N.: Increased Climate Response and Earth System Sensitivity From CCSM4 to CESM2 in Mid-Pliocene Simulations, Journal of Advances in Modeling Earth Systems, 12, https://doi.org/10.1029/2019MS002033, 2020.

Ferrari, R. and Ferreira, D.: What processes drive the ocean heat transport?, Ocean Modelling, 38, 171–186, https://doi.org/10.1016/j.ocemod.2011.02.013, 2011.

780   Foley, K. and Dowsett, H.: Community sourced mid-Piacenzian sea surface temperature (SST) data: U.S. Geological Survey data release, https://doi.org/10.5066/P9YP3DTV, 2019.

Haarsma, R. J., Selten, F. M., and Drijfhout, S. S.: Decelerating Atlantic meridional overturning circulation main cause of future west European summer atmospheric circulation changes, Environmental Research Letters, 10, 094 007, https://doi.org/10.1088/1748-9326/10/9/094007, 2015.

785   Hall, M. M. and Bryden, H. L.: Direct estimates and mechanisms of ocean heat transport, Deep Sea Research Part A. Oceanographic Research Papers, 29, 339–359, https://doi.org/10.1016/0198-0149(82)90099-1, 1982.

Han, Z., Zhang, Q., Li, Q., Feng, R., Haywood, A. M., Tindall, J. C., Hunter, S. J., Otto-Bliesner, B. L., Brady, E. C., Rosenbloom, N., Zhang, Z., Li, X., Guo, C., Nisancioglu, K. H., Stepanek, C., Lohmann, G., Sohl, L. E., Chandler, M. A., Tan, N., Ramstein, G., Baatsen, M. L. J., von der Heydt, A. S., Chandan, D., Peltier, W. R., Williams, C. J. R., Lunt, D. J., Cheng, J., Wen, Q., and Burls, N. J.: Evaluating
790   the large-scale hydrological cycle response within the Pliocene Model Intercomparison Project Phase 2 (PlioMIP2) ensemble, Climate of the Past, 17, 2537–2558, https://doi.org/10.5194/cp-17-2537-2021, 2021.

Haywood, A., Dowsett, H., Dolan, A., Rowley, D., Abe-Ouchi, A., Otto-Bliesner, B., Chandler, M., Hunter, S., Lunt, D., Pound, M., and Salzmann, U.: The Pliocene Model Intercomparison Project (PlioMIP) Phase 2: scientific objectives and experimental design, Climate of the Past, 12, 663–675, https://doi.org/10.5194/cp-12-663-2016, 2016.

795 Haywood, A. M., Dolan, A. M., Pickering, S. J., Dowsett, H. J., McClymont, E. L., Prescott, C. L., Salzmann, U., Hill, D. J., Hunter, S. J., Lunt, D. J., Pope, J. O., and Valdes, P. J.: On the identification of a Pliocene time slice for data–model comparison, Philosophical Transactions of the Royal Society A: Mathematical, Physical and Engineering Sciences, 371, 20120 515, https://doi.org/10.1098/rsta.2012.0515, 2013a.

Haywood, A. M., Hill, D. J., Dolan, A. M., Otto-Bliesner, B. L., Bragg, F., Chan, W.-L., Chandler, M. A., Contoux, C., Dowsett, H. J.,
800 Jost, A., Kamae, Y., Lohmann, G., Lunt, D. J., Abe-Ouchi, A., Pickering, S. J., Ramstein, G., Rosenbloom, N. A., Salzmann, U., Sohl, L., Stepanek, C., Ueda, H., Yan, Q., and Zhang, Z.: Large-scale features of Pliocene climate: results from the Pliocene Model Intercomparison Project, Climate of the Past, 9, 191–209, https://doi.org/10.5194/cp-9-191-2013, 2013b.

Haywood, A. M., Tindall, J. C., Dowsett, H. J., Dolan, A. M., Foley, K. M., Hunter, S. J., Hill, D. J., Chan, W.-L., Abe-Ouchi, A., Stepanek, C., Lohmann, G., Chandan, D., Peltier, W. R., Tan, N., Contoux, C., Ramstein, G., Li, X., Zhang, Z., Guo, C., Nisancioglu, K. H., Zhang,
805 Q., Li, Q., Kamae, Y., Chandler, M. A., Sohl, L. E., Otto-Bliesner, B. L., Feng, R., Brady, E. C., von der Heydt, A. S., Baatsen, M. L. J., and Lunt, D. J.: The Pliocene Model Intercomparison Project Phase 2: large-scale climate features and climate sensitivity, Climate of the Past, 16, 2095–2123, https://doi.org/10.5194/cp-16-2095-2020, 2020.

Hu, A., Meehl, G. A., Han, W., Otto-Bliesner, B., Abe-Ouchi, A., and Rosenbloom, N.: Effects of the Bering Strait closure on AMOC and global climate under different background climates, Progress in Oceanography, 132, 174–196,
810 https://doi.org/10.1016/j.pocean.2014.02.004, 2015.

Huang, B., Thorne, P. W., Banzon, V. F., Boyer, T., Chepurin, G., Lawrimore, J. H., Menne, M. J., Smith, T. M., Vose, R. S., and Zhang, H.-M.: Extended Reconstructed Sea Surface Temperature, Version 5 (ERSSTv5): Upgrades, Validations, and Intercomparisons, Journal of Climate, 30, 8179–8205, https://doi.org/10.1175/JCLI-D-16-0836.1, 2017.

Hunter, S. J., Haywood, A. M., Dolan, A. M., and Tindall, J. C.: The HadCM3 contribution to PlioMIP phase 2, Climate of the Past, 15,
815 1691–1713, https://doi.org/10.5194/cp-15-1691-2019, 2019.

Jackson, L. C., Kahana, R., Graham, T., Ringer, M. A., Woollings, T., Mecking, J. V., and Wood, R. A.: Global and European climate impacts of a slowdown of the AMOC in a high resolution GCM, Climate Dynamics, 45, 3299–3316, https://doi.org/10.1007/s00382-015-2540-2, 2015.

Johns, W. E., Baringer, M. O., Beal, L. M., Cunningham, S. A., Kanzow, T., Bryden, H. L., Hirschi, J. J. M., Marotzke, J., Meinen, C. S., Shaw,
820 B., and Curry, R.: Continuous, Array-Based Estimates of Atlantic Ocean Heat Transport at 26.5°N, Journal of Climate, 24, 2429–2449, https://doi.org/10.1175/2010JCLI3997.1, 2011.

Jüling, A., Zhang, X., Castellana, D., von der Heydt, A. S., and Dijkstra, H. A.: The Atlantic's freshwater budget under climate change in the Community Earth System Model with strongly eddying oceans, Ocean Science, 17, 729–754, https://doi.org/10.5194/os-17-729-2021, 2021.

825 Kim, W. M., Yeager, S., Chang, P., and Danabasoglu, G.: Low-frequency North Atlantic climate variability in the Community Earth System Model large ensemble, Journal of Climate, 31, 787–813, https://doi.org/10.1175/JCLI-D-17-0193.1, 2018.

Li, X., Guo, C., Zhang, Z., Otterå, O. H., and Zhang, R.: PlioMIP2 simulations with NorESM-L and NorESM1-F, Climate of the Past, 16, 183–197, https://doi.org/10.5194/cp-16-183-2020, 2020.

Lohmann, G., Knorr, G., Hossain, A., and Stepanek, C.: Effects of CO2 and Ocean Mixing on Miocene and Pliocene Temperature Gradients, Paleoceanography and Paleoclimatology, 37, https://doi.org/10.1029/2020PA003953, 2022.

Lurton, T., Balkanski, Y., Bastrikov, V., Bekki, S., Bopp, L., Braconnot, P., Brockmann, P., Cadule, P., Contoux, C., Cozic, A., Cugnet, D., Dufresne, J., Éthé, C., Foujols, M., Ghattas, J., Hauglustaine, D., Hu, R., Kageyama, M., Khodri, M., Lebas, N., Levavasseur, G., Marchand, M., Ottlé, C., Peylin, P., Sima, A., Szopa, S., Thiéblemont, R., Vuichard, N., and Boucher, O.: Implementation of the CMIP6 Forcing Data in the IPSL-CM6A-LR Model, Journal of Advances in Modeling Earth Systems, 12, https://doi.org/10.1029/2019MS001940, 2020.

McClymont, E. L., Ford, H. L., Ho, S. L., Tindall, J. C., Haywood, A. M., Alonso-Garcia, M., Bailey, I., Berke, M. A., Littler, K., Patterson, M. O., Petrick, B., Peterse, F., Ravelo, A. C., Risebrobakken, B., De Schepper, S., Swann, G. E. A., Thirumalai, K., Tierney, J. E., van der Weijst, C., White, S., Abe-Ouchi, A., Baatsen, M. L. J., Brady, E. C., Chan, W.-L., Chandan, D., Feng, R., Guo, C., von der Heydt, A. S., Hunter, S., Li, X., Lohmann, G., Nisancioglu, K. H., Otto-Bliesner, B. L., Peltier, W. R., Stepanek, C., and Zhang, Z.: Lessons from a high-CO2 world: an ocean view from $\sim$ 3 million years ago, Climate of the Past, 16, 1599–1615, https://doi.org/10.5194/cp-16-1599-2020, 2020.

Müller, P. J., Kirst, G., Ruhland, G., Von Storch, I., and Rosell-Melé, A.: Calibration of the alkenone paleotemperature index U37K′ based on core-tops from the eastern South Atlantic and the global ocean (60° N-60° S), Geochimica et Cosmochimica Acta, 62, 1757–1772, https://doi.org/10.1016/S0016-7037(98)00097-0, 1998.

Oldeman, A.: arthuroldeman/pliomip2-enso: v1.0, pliomip2_enso, Zenodo [code], https://doi.org/10.5281/zenodo.5718483,2021, 2021.

Otto-Bliesner, B. L., Jahn, A., Feng, R., Brady, E. C., Hu, A., and Löfverström, M.: Amplified North Atlantic warming in the late Pliocene by changes in Arctic gateways, Geophysical Research Letters, 44, 957–964, https://doi.org/10.1002/2016GL071805, 2017.

Pagani, M., Liu, Z., LaRiviere, J., and Ravelo, A. C.: High Earth-system climate sensitivity determined from Pliocene carbon dioxide concentrations, Nature Geoscience, 3, 27–30, https://doi.org/10.1038/ngeo724, 2010.

Rahmstorf, S.: On the freshwater forcing and transport of the Atlantic thermohaline circulation, Climate Dynamics, 12, 799–811, https://doi.org/10.1007/s003820050144, 1996.

Ravelo, A. C. and Andreasen, D. H.: Enhanced circulation during a warm period, Geophysical Research Letters, 27, 1001–1004, https://doi.org/10.1029/1999GL007000, 2000.

Raymo, M., Grant, B., Horowitz, M., and Rau, G.: Mid-Pliocene warmth: stronger greenhouse and stronger conveyor, Marine Micropaleontology, 27, 313–326, https://doi.org/10.1016/0377-8398(95)00048-8, 1996.

Roquet, F., Madec, G., McDougall, T. J., and Barker, P. M.: Accurate polynomial expressions for the density and specific volume of seawater using the TEOS-10 standard, Ocean Modelling, 90, 29–43, https://doi.org/10.1016/j.ocemod.2015.04.002, 2015.

Rose, B. E. J. and Ferreira, D.: Ocean Heat Transport and Water Vapor Greenhouse in a Warm Equable Climate: A New Look at the Low Gradient Paradox, Journal of Climate, 26, 2117–2136, https://doi.org/10.1175/JCLI-D-11-00547.1, 2012.

Saba, V. S., Griffies, S. M., Anderson, W. G., Winton, M., Alexander, M. A., Delworth, T. L., Hare, J. A., Harrison, M. J., Rosati, A., Vecchi, G. A., and Zhang, R.: Enhanced warming of the Northwest Atlantic Ocean under climate change, Journal of Geophysical Research: Oceans, 121, 118–132, https://doi.org/10.1002/2015JC011346, 2016.

Schoonover, J., Dewar, W. K., Wienders, N., and Deremble, B.: Local Sensitivities of the Gulf Stream Separation, Journal of Physical Oceanography, 47, 353–373, https://doi.org/10.1175/JPO-D-16-0195.1, 2017.

Seki, O., Foster, G. L., Schmidt, D. N., Mackensen, A., Kawamura, K., and Pancost, R. D.: Alkenone and boron-based Pliocene pCO2 records, Earth and Planetary Science Letters, 292, 201–211, https://doi.org/10.1016/j.epsl.2010.01.037, 2010.

Stepanek, C., Samakinwa, E., Knorr, G., and Lohmann, G.: Contribution of the coupled atmosphere–ocean–sea ice–vegetation model COS-MOS to the PlioMIP2, Climate of the Past, 16, 2275–2323, https://doi.org/10.5194/cp-16-2275-2020, 2020.

Stouffer, R. J., Yin, J., Gregory, J. M., Dixon, K. W., Spelman, M. J., Hurlin, W., Weaver, A. J., Eby, M., Flato, G. M., Hasumi, H., Hu, A.,

870   Jungclaus, J. H., Kamenkovich, I. V., Levermann, A., Montoya, M., Murakami, S., Nawrath, S., Oka, A., Peltier, W. R., Robitaille, D. Y., Sokolov, A., Vettoretti, G., and Weber, S. L.: Investigating the Causes of the Response of the Thermohaline Circulation to Past and Future Climate Changes, Journal of Climate, 19, 1365–1387, https://doi.org/10.1175/JCLI3689.1, 2006.

Talley, L. D.: Shallow, Intermediate, and Deep Overturning Components of the Global Heat Budget, Journal of Physical Oceanography, 33, 530–560, https://doi.org/10.1175/1520-0485(2003)033<0530:SIADOC>2.0.CO;2, 2003.

875   Tan, N., Contoux, C., Ramstein, G., Sun, Y., Dumas, C., Sepulchre, P., and Guo, Z.: Modeling a modern-like pCO2 warm period (Marine Isotope Stage KM5c) with two versions of an Institut Pierre Simon Laplace atmosphere–ocean coupled general circulation model, Climate of the Past, 16, 1–16, https://doi.org/10.5194/cp-16-1-2020, 2020.

Thorpe, R. B., Gregory, J. M., Johns, T. C., Wood, R. A., and Mitchell, J. F. B.: Mechanisms Determining the Atlantic Thermohaline Circulation Response to Greenhouse Gas Forcing in a Non-Flux-Adjusted Coupled Climate Model, Journal of Climate, 14, 3102–3116,

880   https://doi.org/10.1175/1520-0442(2001)014<3102:MDTATC>2.0.CO;2, 2001.

Tierney, J. E., Haywood, A. M., Feng, R., Bhattacharya, T., and Otto-Bliesner, B. L.: Pliocene Warmth Consistent With Greenhouse Gas Forcing, Geophysical Research Letters, 46, 9136–9144, https://doi.org/10.1029/2019GL083802, 2019.

Treguier, A. M., Deshayes, J., Lique, C., Dussin, R., and Molines, J. M.: Eddy contributions to the meridional transport of salt in the North Atlantic, Journal of Geophysical Research: Oceans, 117, https://doi.org/10.1029/2012JC007927, 2012.

885   Vallis, G. K. and Farneti, R.: Meridional energy transport in the coupled atmosphere-ocean system: scaling and numerical experiments, Quarterly Journal of the Royal Meteorological Society, 135, 1643–1660, https://doi.org/10.1002/qj.498, 2009.

Viebahn, J. P., von der Heydt, A. S., Le Bars, D., and Dijkstra, H. A.: Effects of Drake Passage on a strongly eddying global ocean, Paleoceanography, 31, 564–581, https://doi.org/10.1002/2015PA002888, 2016.

Wang, C., Dong, S., and Munoz, E.: Seawater density variations in the North Atlantic and the Atlantic meridional overturning circulation,

890   Climate Dynamics, 34, 953–968, https://doi.org/10.1007/s00382-009-0560-5, 2010.

Weiffenbach, J.: jweiffenbach/pliomip2-amoc: v1.1, pliomip2-amoc, Zenodo [code], https://doi.org/DOI:10.5281/zenodo.7288756,2022, 2022.

Weijer, W., Cheng, W., Drijfhout, S. S., Fedorov, A. V., Hu, A., Jackson, L. C., Liu, W., McDonagh, E. L., Mecking, J. V., and Zhang, J.: Stability of the Atlantic Meridional Overturning Circulation: A Review and Synthesis, Journal of Geophysical Research: Oceans, 124,

895   5336–5375, https://doi.org/10.1029/2019JC015083, 2019.

Weijer, W., Cheng, W., Garuba, O. A., Hu, A., and Nadiga, B. T.: CMIP6 Models Predict Significant 21st Century Decline of the Atlantic Meridional Overturning Circulation, Geophysical Research Letters, 47, https://doi.org/10.1029/2019GL086075, 2020.

Williams, C. J., Sellar, A. A., Ren, X., Haywood, A. M., Hopcroft, P., Hunter, S. J., Roberts, W. H., Smith, R. S., Stone, E. J., Tindall, J. C., and others: Simulation of the mid-Pliocene Warm Period using HadGEM3: experimental design and results from model–model and

900   model–data comparison, Climate of the Past, 17, 2139–2163, https://doi.org/10.5194/cp-17-2139-2021, 2021.

Yang, H. and Dai, H.: Effect of wind forcing on the meridional heat transport in a coupled climate model: equilibrium response, Climate Dynamics, 45, 1451–1470, https://doi.org/10.1007/s00382-014-2393-0, 2015.

Yang, H., Li, Q., Wang, K., Sun, Y., and Sun, D.: Decomposing the meridional heat transport in the climate system, Climate Dynamics, 44, 2751–2768, https://doi.org/10.1007/s00382-014-2380-5, 2015.

905 Zhang, Q., Berntell, E., Axelsson, J., Chen, J., Han, Z., de Nooijer, W., Lu, Z., Li, Q., Zhang, Q., Wyser, K., and Yang, S.: Simulating the mid-Holocene, last interglacial and mid-Pliocene climate with EC-Earth3-LR, Geoscientific Model Development, 14, 1147–1169, https://doi.org/10.5194/gmd-14-1147-2021, 2021a.

Zhang, R., Sutton, R., Danabasoglu, G., Kwon, Y.-O., Marsh, R., Yeager, S. G., Amrhein, D. E., and Little, C. M.: A review of the role of the Atlantic meridional overturning circulation in Atlantic multidecadal variability and associated climate impacts, Reviews of Geophysics,
910 57, 316–375, https://doi.org/10.1029/2019RG000644, 2019.

Zhang, Z., Li, X., Guo, C., Otterå, O. H., Nisancioglu, K. H., Tan, N., Contoux, C., Ramstein, G., Feng, R., Otto-Bliesner, B. L., Brady, E., Chandan, D., Peltier, W. R., Baatsen, M. L. J., von der Heydt, A. S., Weiffenbach, J. E., Stepanek, C., Lohmann, G., Zhang, Q., Li, Q., Chandler, M. A., Sohl, L. E., Haywood, A. M., Hunter, S. J., Tindall, J. C., Williams, C., Lunt, D. J., Chan, W.-L., and Abe-Ouchi, A.: Mid-Pliocene Atlantic Meridional Overturning Circulation simulated in PlioMIP2, Climate of the Past, 17, 529–543,
915 https://doi.org/https://doi.org/10.5194/cp-17-529-2021, 2021b.

Supplementary Tables and Figures
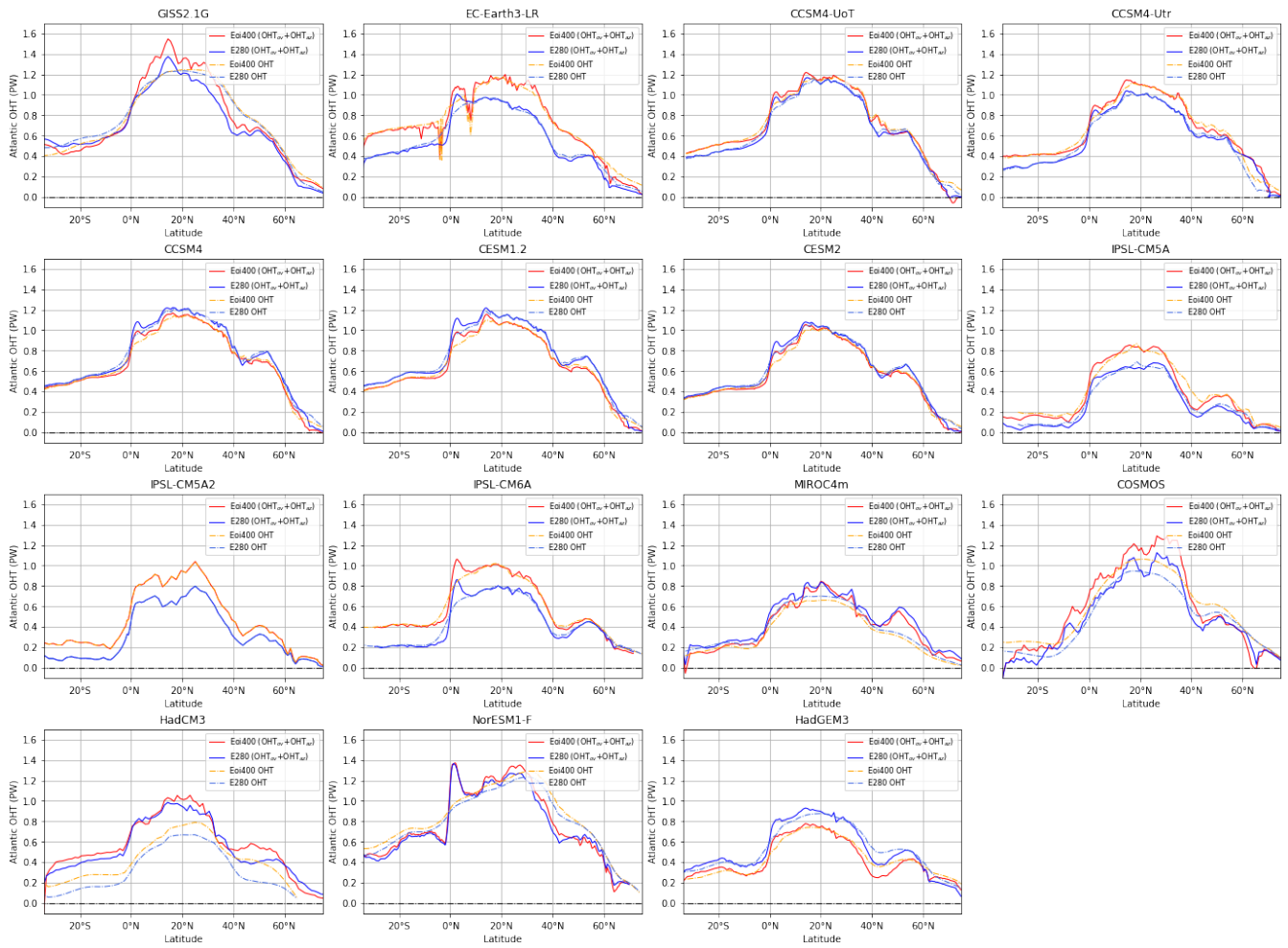
Figure S1. Comparison of total Atlantic OHT with the sum of the overturning and gyre Atlantic OHT components (OHT$_{ov}$+OHT$_{az}$) for all models. Solid lines represent the sum of the overturning and gyre Atlantic OHT component and dashed lines represent the total Atlantic OHT.
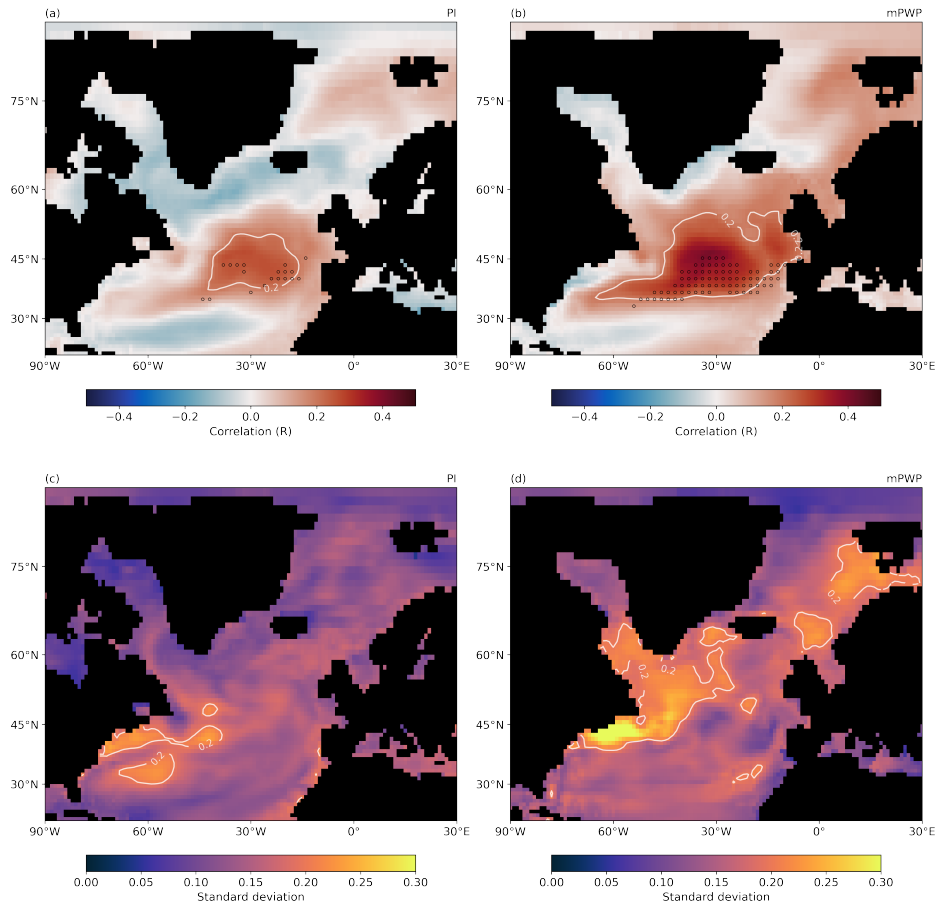
Figure S2. (a) Multi-model mean correlation between the annual AMOC strength and annual SSTs for the pre-industrial simulations. (b) Same as (a) for the mid-Pliocene simulations. Stippling indicates 12 or more models agree on the sign of the correlation. White contours show a positive correlation of $R = 0.2$. (c) Standard deviation from the pre-industrial MMM by individual models. (d) Standard deviation from the mid-Pliocene MMM by individual models. White contours show a standard deviation of 0.2. HadGEM3 is excluded from the MMM and standard deviation calculations.
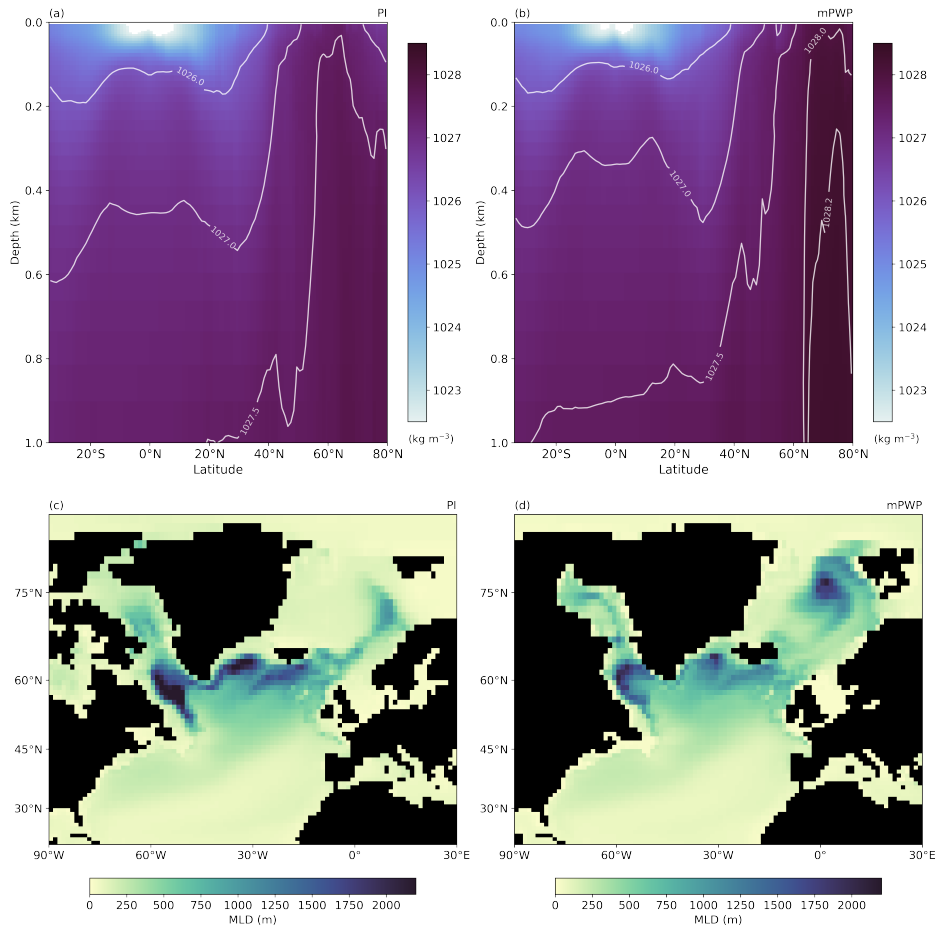
Figure S3. (a) Atlantic zonal mean potential density in top 1 km in the GISS2.1G pre-industrial simulation. (b) Same as (a) for the mid-Pliocene simulation. (c) Average mixed layer depth in the GISS2.1G pre-industrial simulation. (d) Same as (c) for the mid-Pliocene simulation.
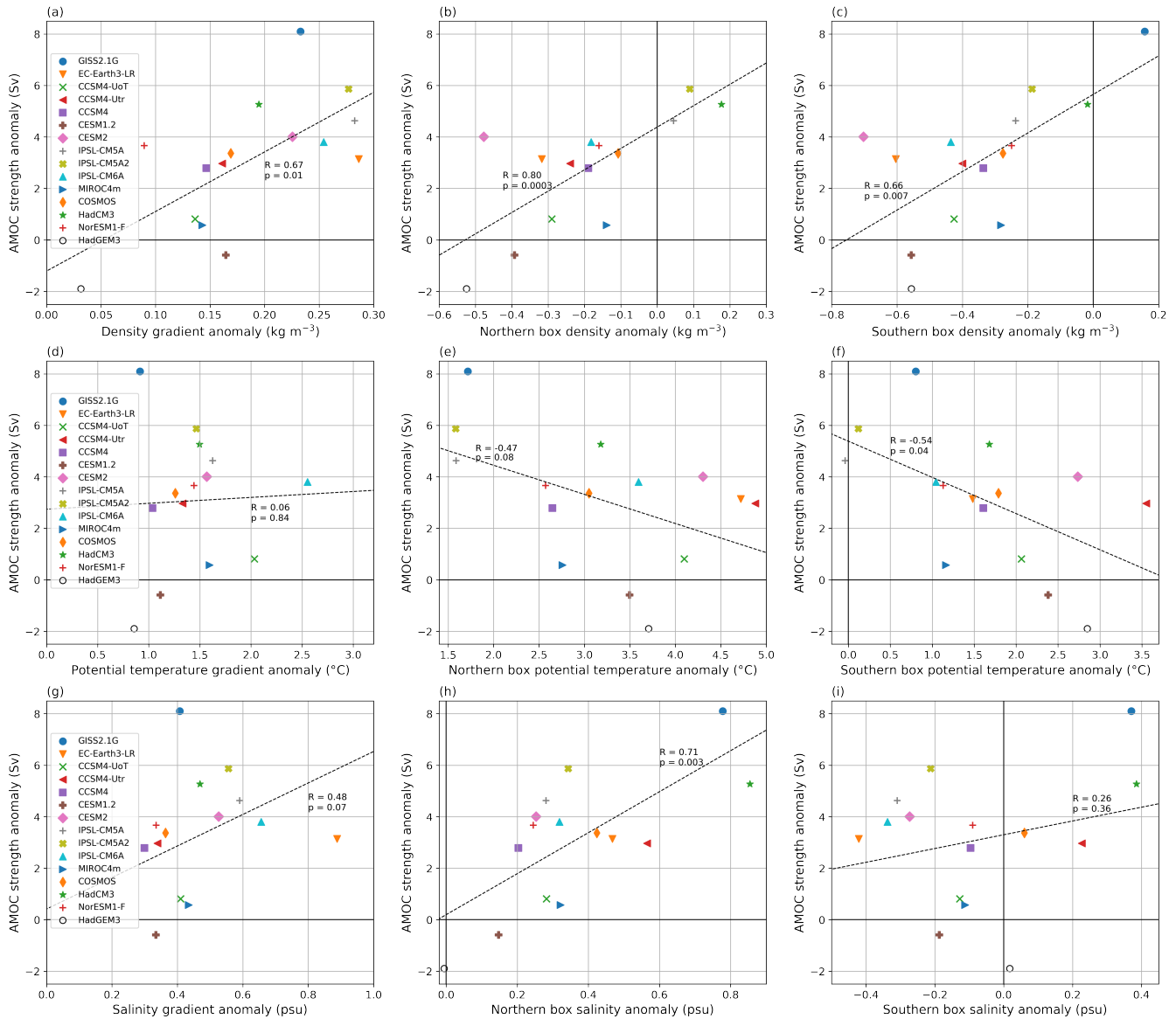
Figure S4. (a) Same as Figure 4c: Individual model mPWP-PI AMOC strength anomaly plotted against the mPWP-PI anomaly in meridional gradient of the top 1 km Atlantic potential density. (b) Individual model mPWP-PI AMOC strength anomaly plotted against the mPWP-PI top 1 km 50-70°N (50-80°N for GISS2.1G) average potential density anomaly. (c) Individual model mPWP-PI AMOC strength anomaly plotted against the mPWP-PI top 1 km 10-30°S average potential density anomaly. (d)-(f) Same as (a)-(c) for potential temperature. (g)-(i) Same as (a)-(c) for salinity. The meridional gradient is defined as the difference between the 50-70°N (50-80°N for GISS2.1G) average and 10-30°S average (latitude bands are indicated by grey shading in Figure 4b).
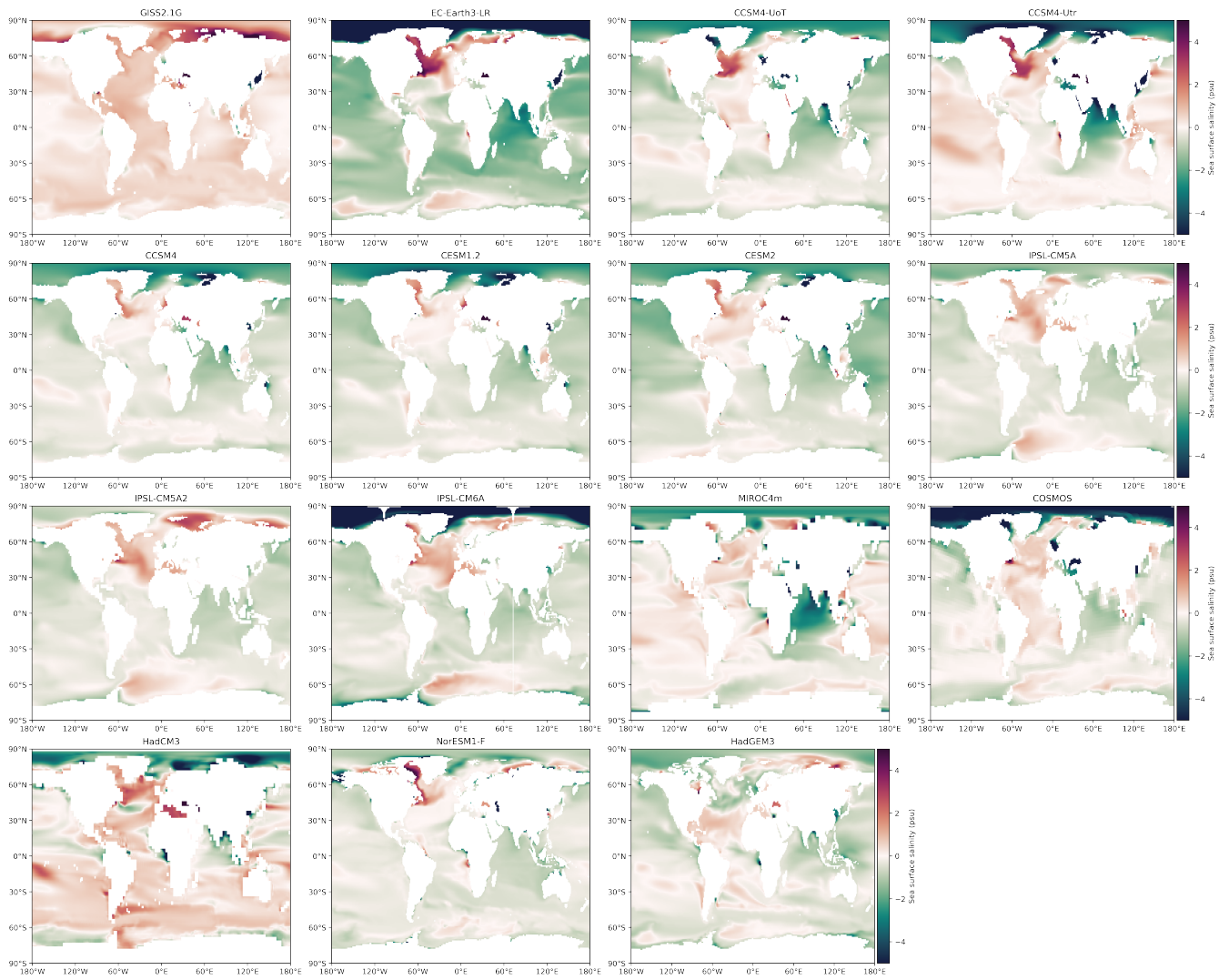
Figure S5. Individual model mPWP-PI difference in sea surface salinity.
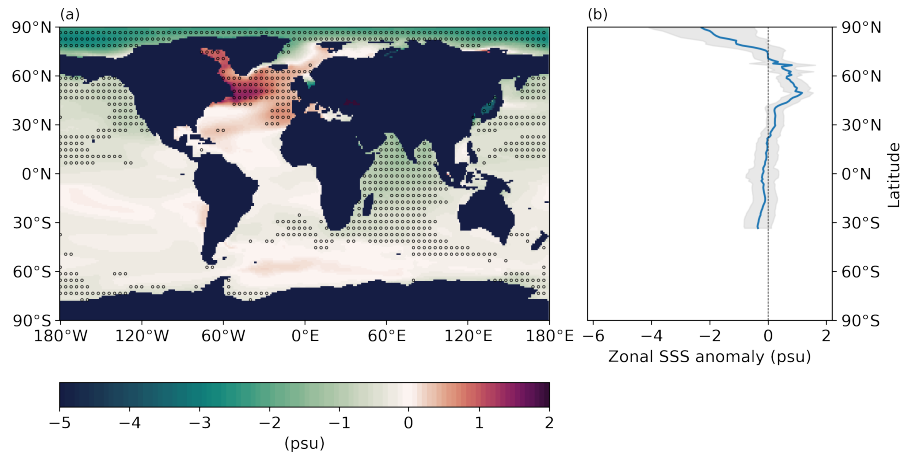
Figure S6. (a) Multi-model mean mPWP-PI difference in top 100 m average salinity. Stippling indicates that 12 or more models agree on the sign of the difference. (b) Atlantic zonal mean salinity difference. The shading indicates one standard deviation from the MMM by individual models, excluding HadGEM3.
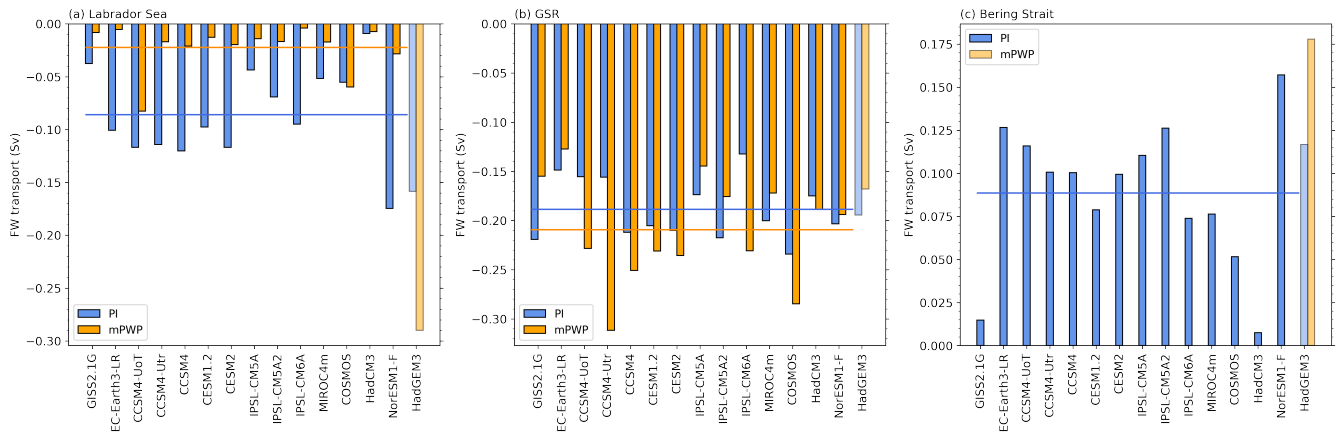
Figure S7. Mean freshwater transport (Sv) in pre-industrial and mid-Pliocene at 62°N (a) into the Labrador Sea and (b) across the GSR. (c) Mean freshwater transport (Sv) through the Bering Strait in the pre-industrial (and mid-Pliocene for HadGEM3). Horizontal lines indicate the MMM transports in the pre-industrial and mid-Pliocene, excluding HadGEM3.
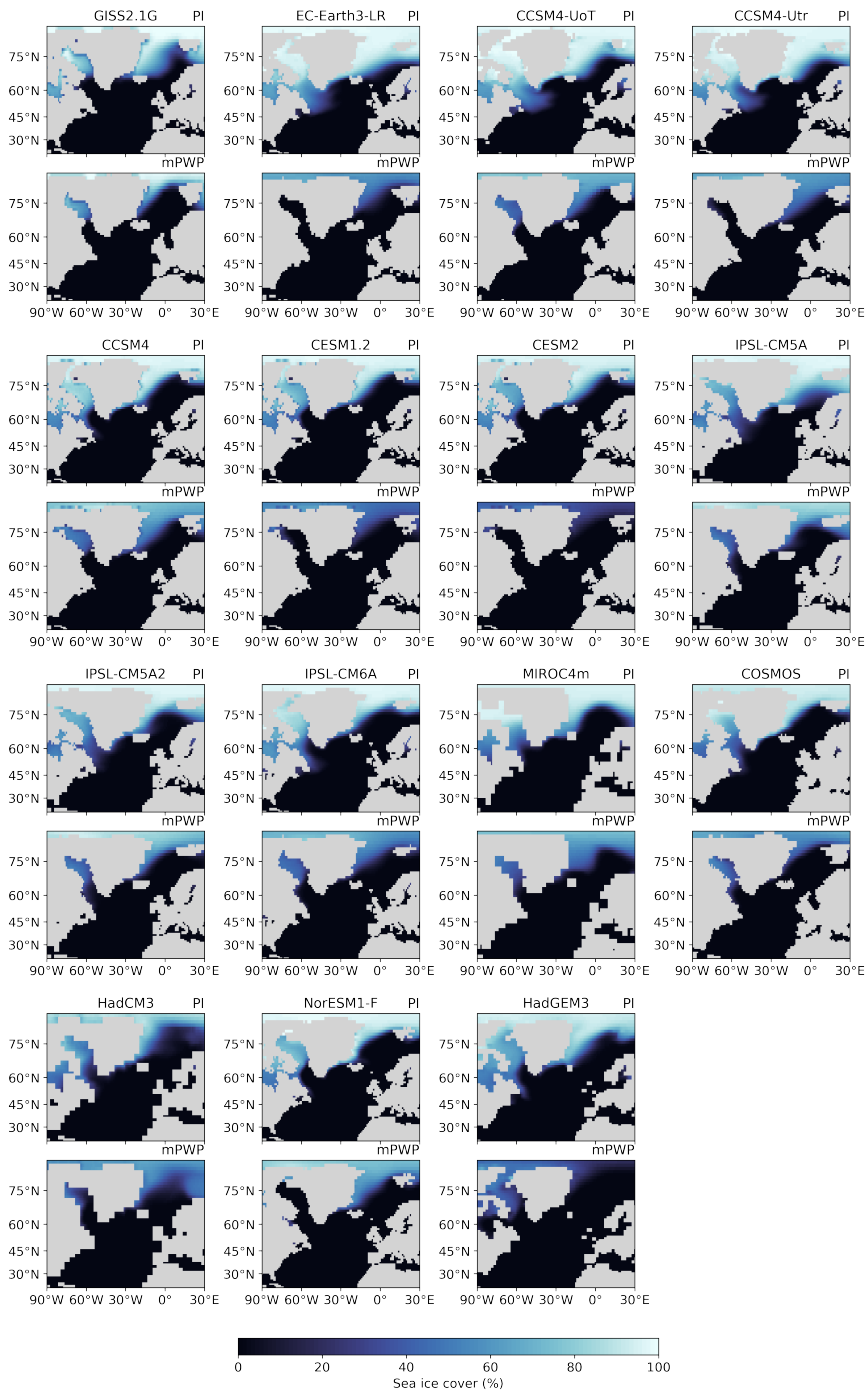
Figure S8. Individual model annual mean sea-ice coverage (%), interpolated to a regular 1x1° grid. The top panel for each model shows the results for the pre-industrial and the bottom panel for the mid-Pliocene. The land-sea masks as shown are not necessarily identical to those of the models due to interpolation.
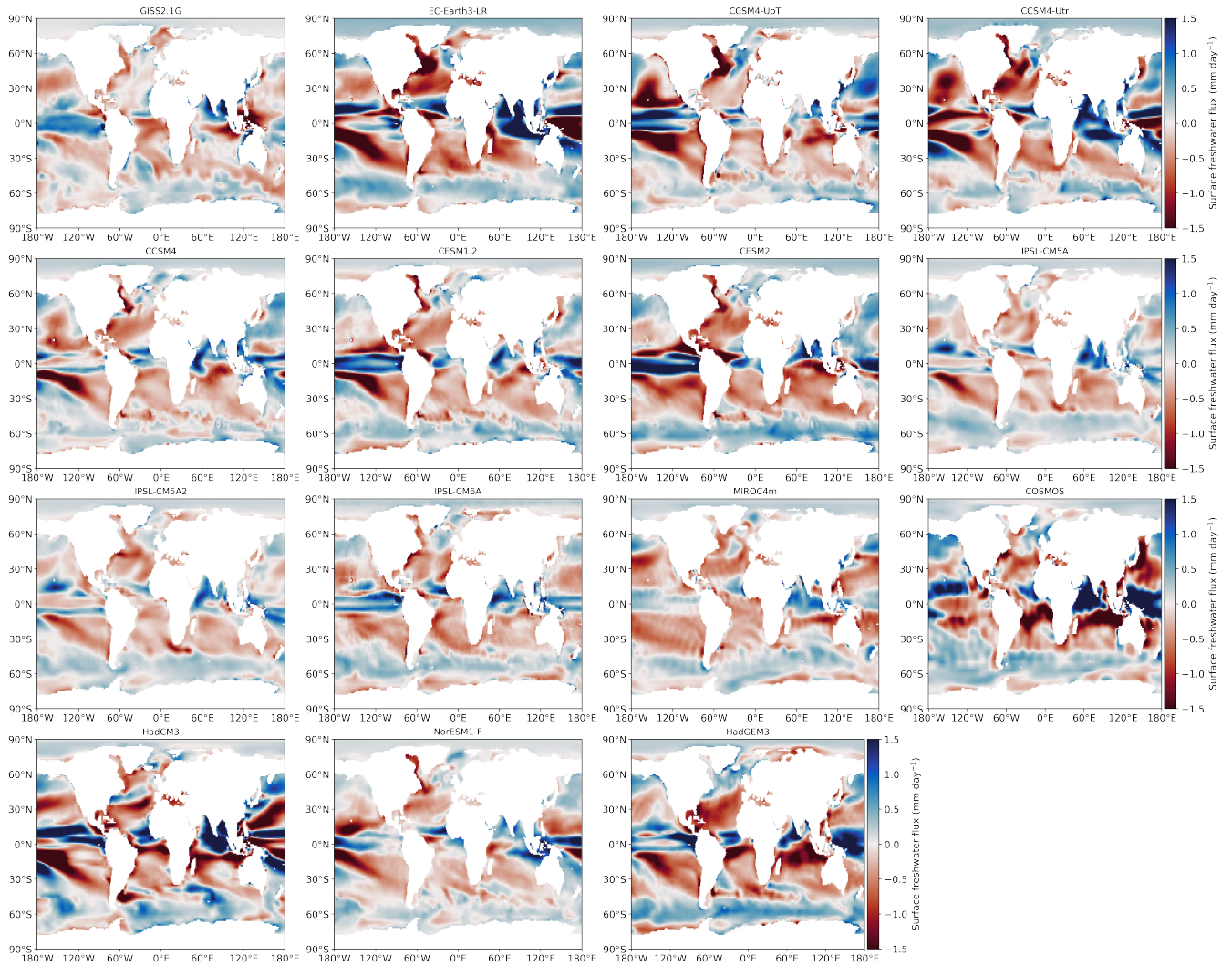
Figure S9. ~~Comparison of total Atlantic OHT with the sum of the overturning and gyre Atlantic OHT components~~ Individual model mPWP-PI difference in surface freshwater flux (~~OHT$_{ov}$+OHT$_{az}$~~PmE)~~for all models.Solid lines represent the sum of the overturning and gyre Atlantic OHT component and dashed lines represent the total Atlantic OHT.~~
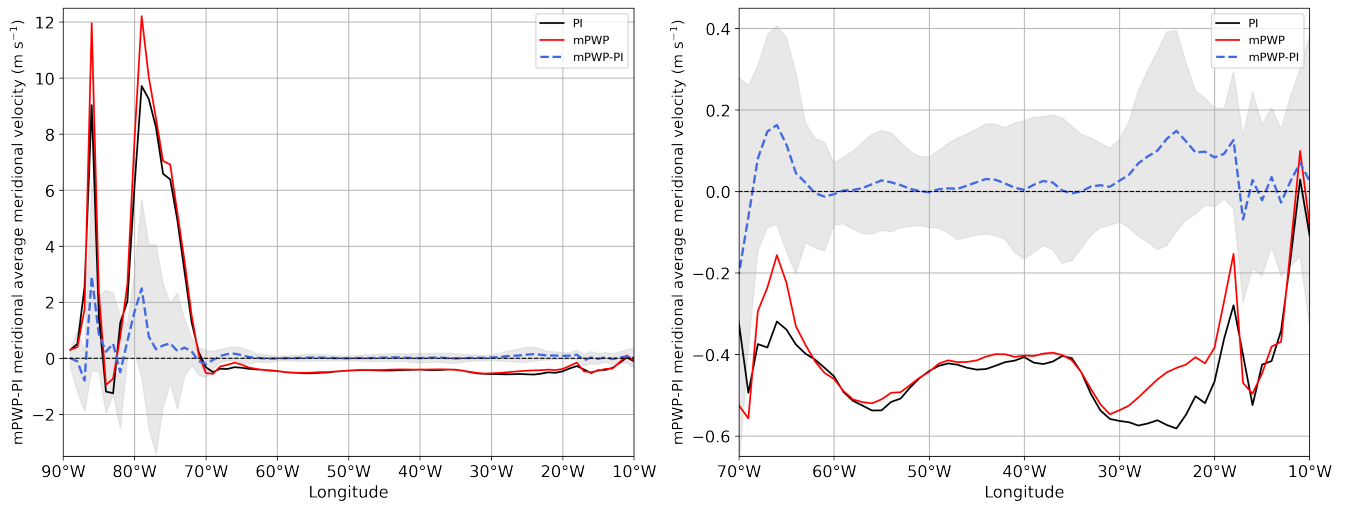
Figure S10. (a) MMM top 500 m Atlantic ocean meridional velocity, averaged over 20-40°N, in the ~~PI~~ pre-industrial and ~~mPWP~~mid-Pliocene, as well as the mPWP-PI anomaly. Grey shading indicates one standard deviation from the MMM anomaly by individual models. (b) Same as (a) but with adapted scaling to show differences in the 10−70°W longitude band.

Table S1. SST proxy data and MMM at North Atlantic sites. FD19-$U_{37}^{k'}$ refers to the Foley and Dowsett (2019) data, M20-$U_{37}^{k'}$ and M20-Mg/Ca to the McClymont et al. (2020) data. SST proxy mPWP-PI anomalies are computed with pre-industrial ERSST5 data (Huang et al., 2017).

Site	Proxy/MMM	mPWP (°C)	mPWP-PI (°C)	MMM - proxy mPWP (°C)	MMM - proxy mPWP-PI (°C)
603	M20-Mg/Ca	20.4	-1.8	4.7	3.9
	MMM	25.1	2.1		
607/1313	FD19-$U_{37}^{k'}$	21.2	3.4	-1.4	-0.4
	FD19-$U_{37}^{k'}$	20.9	3.1	-1.1	-0.1
	M20-$U_{37}^{k'}$	20.9	3.1	-1.1	-0.1
	M20-$U_{37}^{k'}$	20.3	2.6	-0.5	0.4
	M20-Mg/Ca	22.2	4.5	-2.4	-1.5
	MMM	19.8	3.0		
609	FD19-$U_{37}^{k'}$	18.5	5.1	-3.3	-1.2
	FD19-$U_{37}^{k'}$	17.2	3.8	-2	0.1
	M20-$U_{37}^{k'}$	17.1	3.7	-1.9	0.2
	M20-Mg/Ca	11.7	-1.7	3.5	5.6
	MMM	15.2	3.9		
982	FD19-$U_{37}^{k'}$	17.2	6.5	-2.9	-2.2
	M20-$U_{37}^{k'}$	16.6	5.9	-2.3	-1.6
	MMM	14.3	4.3		
642	FD19-$U_{37}^{k'}$	13.8	7.0	-4.2	-2.9
	M20-$U_{37}^{k'}$	13.2	6.4	-3.6	-2.3
	MMM	9.6	4.1		
907	M20-$U_{37}^{k'}$	3.2	1.7	1.1	2.3
	MMM	4.3	4.0		

Table S2. AMOC-SST correlation map (Figure 3) data. The area of positive correlation is shown as the percentage of significant positively correlated grid cells with respect to the total number of extratropical North Atlantic ($30°$N-$80°$N) grid cells. The mean and maximum correlation are respectively the mean and the maximum of all significant positively correlated grid cells in the extratropical North Atlantic.

Model	Area (%)		Mean		Maximum	
	E^{280}	Eoi^{400}	E^{280}	Eoi^{400}	E^{280}	Eoi^{400}
GISS-E2.1G	28	61	0.35	0.38	0.69	0.60
EC-Earth3-LR	1	65	0.25	0.32	0.36	0.54
CCSM4-UoT	30	31	0.34	0.36	0.54	0.62
CCSM4-Utr	11	52	0.28	0.40	0.40	0.72
CCSM4	19	27	0.31	0.27	0.46	0.43
CESM1.2	17	24	0.31	0.31	0.50	0.48
CESM2	40	2	0.35	0.22	0.55	0.26
IPSL-CM6A	32	23	0.36	0.35	0.54	0.56
MIROC4m	9	26	0.27	0.33	0.47	0.55
COSMOS	12	58	0.25	0.39	0.38	0.65
HadCM3	20	52	0.29	0.36	0.49	0.61
NorESM1-F	20	20	0.27	0.29	0.37	0.45
HadGEM3	29	12	0.26	0.29	0.36	0.50
MMM[*]	20	37	0.30	0.33	0.48	0.54

[*] HadGEM3 is excluded from the MMM.